Accepted Manuscript

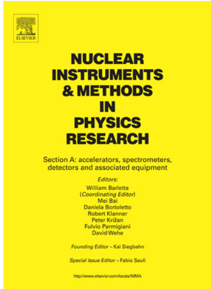

Design and performance of the spin asymmetries on the nucleon experiment

J.D. Maxwell, W.R. Armstrong, S. Choi, M.K. Jones, H.-K. Kang, A. Liyanage, Z.-E. Meziani, J. Mulholland, L. Ndukum, O. Rondón, A. Ahmidouch, I. Albayrak, A. Asaturyan, O. Ates, H. Baghdasaryan, W. Boeglin, P. Bosted, E. Brash, J. Brock, C. Butuceanu, M. Bychkov, C. Carlin, P. Carter, C. Chen, J.-P. Chen, M.E. Christy, S. Covrig, D. Crabb, S. Danagoulian, A. Daniel, A.M. Davidenko, B. Davis, D. Day, W. Deconinck, A. Deur, J. Dunne, D. Dutta, L. El Fassi, M. Elaasar, C. Ellis, R. Ent, D. Flay, E. Frlez, D. Gaskell, O. Geagla, J. German, R. Gilman, T. Gogami, J. Gomez, Y.M. Goncharenko, O. Hashimoto, D.W. Higinbotham, T. Horn, G.M. Huber, M. Jones, N. Kalantarians, H. Kang, D. Kawama, C. Keith, C. Keppel, M. Khandaker, Y. Kim, P.M. King, M. Kohl, K. Kovacs, V.I. Kravtsov, V. Kubarovsky, Y. Li, N. Liyanage, W. Luo, V. Mamyan, P. Markowitz, T. Maruta, D. Meekins, Y.M. Melnik, A. Mkrtchyan, H. Mkrtchyan, V.V. Mochalov, P. Monaghan, A. Narayan, S.N. Nakamura, A. Nuruzzaman, L. Pentchev, D. Pocanic, M. Posik, A. Puckett, X. Qiu, J. Reinhold, S. Riordan, J. Roche, B. Sawatzky, M. Shabestari, K. Slifer, G. Smith, L. Soloviev, P. Solvignon, V. Tadevosyan, L. Tang, A. Vasiliev, M. Veilleux, T. Walton, F. Wesselmann, S.A. Wood, H. Yao, Z. Ye, L. Zhu

PII: S0168-9002(17)31362-1
DOI: https://doi.org/10.1016/j.nima.2017.12.008
Reference: NIMA 60349

To appear in: *Nuclear Inst. and Methods in Physics Research, A*

Received date : 28 November 2017
Revised date : 4 December 2017
Accepted date : 4 December 2017

Design and Performance of the Spin Asymmetries on the Nucleon Experiment

J.D. Maxwell[a,*], W.R. Armstrong[b,z], S. Choi[e], M.K. Jones[a], H.-K. Kang[e], A. Liyanage[f], Z.-E. Meziani[b], J. Mulholland[c], L. Ndukum[g], O. Rondón[c], A. Ahmidouch[h], I. Albayrak[f], A. Asaturyan[i], O. Ates[f], H. Baghdasaryan[c], W. Boeglin[j], P. Bosted[a], E. Brash[k,a], J. Brock[a], C. Butuceanu[m], M. Bychkov[c], C. Carlin[a], P. Carter[k], C. Chen[f], J.-P. Chen[a], M.E. Christy[f], S. Covrig[a], D. Crabb[c], S. Danagoulian[h], A. Daniel[n], A.M. Davidenko[o], B. Davis[h], D. Day[c], W. Deconinck[d], A. Deur[a], J. Dunne[g], D. Dutta[g], L. El Fassi[g,p], M. Elaasar[x], C. Ellis[a], R. Ent[a], D. Flay[b], E. Frlez[c], D. Gaskell[a], O. Geagla[c], J. German[h], R. Gilman[p], T. Gogami[s], J. Gomez[a], Y.M. Goncharenko[o], O. Hashimoto[s,**], D.W. Higinbotham[a], T. Horn[a,y], G.M. Huber[m], M. Jones[c], N. Kalantarians[q], H Kang[e], D. Kawama[s], C. Keith[a], C. Keppel[a], M. Khandaker[r], Y. Kim[e], P.M. King[n], M. Kohl[f], K. Kovacs[c], V.I. Kravtsov[o], V. Kubarovsky[u], Y. Li[f], N. Liyanage[c], W. Luo[v], V. Mamyan[c], P. Markowitz[j], T. Maruta[t], D. Meekins[a], Y.M. Melnik[o], A. Mkrtchyan[i], H. Mkrtchyan[i], V.V. Mochalov[o], P. Monaghan[f], A. Narayan[g], S.N. Nakamura[s], A. Nuruzzaman[g], L. Pentchev[d], D. Pocanic[c], M. Posik[b], A. Puckett[w], X. Qiu[f], J. Reinhold[j], S. Riordan[z], J. Roche[n], B. Sawatzky[b], M. Shabestari[c,g], K. Slifer[l], G. Smith[a], L. Soloviev[o], P. Solvignon[l,**], V. Tadevosyan[i], L. Tang[f], A. Vasiliev[o], M. Veilleux[k], T. Walton[f], F. Wesselmann[1], S.A. Wood[a], H. Yao[b], Z. Ye[f], L. Zhu[f]

[a] *Thomas Jefferson National Accelerator Facility, Newport News, VA*
[b] *Temple University, Philadelphia, PA*
[c] *University of Virginia, Charlottesville, VA*
[d] *William & Mary, Williamsburg, VA*
[e] *Seoul National University, Seoul, Korea*
[f] *Hampton University, Hampton, VA*
[g] *Mississippi State University, Starkville, MS*
[h] *North Carolina A&M State University, Greensboro, NC*
[i] *Yerevan Physics Institute, Yerevan, Armenia*
[j] *Florida International University, Miami, FL*
[k] *Christopher Newport University, Newport News, VA*
[l] *University of New Hampshire, Durham, NH*
[m] *University of Regina, Regina, SK*
[n] *Ohio University, Athens, OH*
[o] *Institute for High Energy Physics, Protvino, Moscow Region, Russia*
[p] *Rutgers University, New Brunswick, NJ*
[q] *Virginia Union University, Richmond, VA*
[r] *Norfolk State University, Norfolk, VA*
[s] *Tohoku University, Sendai, Japan*
[t] *KEK, Tsukuba, Japan*
[u] *Rensselaer Polytechnic Institute, Troy, NY*

*Corresponding author
**Deceased
Email address: jmaxwell@jlab.org (J.D. Maxwell)

[v]Lanzhou University, Gansu, China
[w]University of Connecticut, Storrs, CT
[x]Southern University at New Orleans, New Orleans, LA
[y]Catholic University of America, Washington, DC
[z]Argonne National Laboratory, Argonne, IL

Abstract

The Spin Asymmetries of the Nucleon Experiment (SANE) performed inclusive, double-polarized electron scattering measurements of the proton at the Continuous Electron Beam Accelerator Facility at Jefferson Lab. A novel detector array observed scattered electrons of four-momentum transfer $2.5 < Q^2 < 6.5\,\mathrm{GeV}^2$ and Bjorken scaling $0.3 < x < 0.8$ from initial beam energies of 4.7 and 5.9 GeV. Employing a polarized proton target whose magnetic field direction could be rotated with respect to the incident electron beam, both parallel and near perpendicular spin asymmetries were measured, allowing model-independent access to transverse polarization observables A_1, A_2, g_1, g_2 and moment d_2 of the proton. This document summarizes the operation and performance of the polarized target, polarized electron beam, and novel detector systems used during the course of the experiment, and describes analysis techniques utilized to access the physics observables of interest.

Keywords: Deep inelastic scattering, Spin asymmetries, Polarized target, Electron detector

1. Introduction

Deep-inelastic leptonic scattering has driven the study of nucleon spin structure as the cleanest probe available to hadronic physics. Inclusive spin asymmetry measurements at high x offer a particularly clear view of nucleon structure where the influence of sea quarks falls away. The Spin Asymmetries of the Nucleon Experiment (SANE) was devised to precisely measure inclusive double-spin asymmetries A_1^p and A_2^p in the deep-inelastic region of final state invariant mass W and in a wide range of x, allowing direct access to spin structure functions g_1^p and the higher-twist dependent g_2^p, revealing trends as x approaches unity, and connecting spin structure function moments to lattice QCD calculations. Where a thorough exploration of these asymmetries with traditional, narrow-acceptance spectrometer techniques would be a protracted, expensive effort, SANE viewed a wide kinematic range using a novel, non-magnetic, high-acceptance electron detector array. This array utilized the drift space between a Cherenkov detector and an electromagnetic calorimeter to create a "telescope" to isolate electron events produced in the target from possible background produced elsewhere along the beamline. To access both spin asymmetries in a model independent way, a polarized proton target was needed which could provide both longitudinal and the more challenging transverse target orientation components.

SANE was performed in Hall C of the Thomas Jefferson National Accelerator Facility from January to March of 2009. A polarized electron beam at energies of 4.7 or 5.9 GeV was incident on a solid, polarized proton target to produce spin asymmetries with the target polarized parallel to the beam, or nearly perpendicular (80°) to it. Scattered electrons were observed using Hall C's standard High Momentum Spectrometer (HMS), as well as a novel detector system, the Big Electron Telescope Array (BETA), resulting in a kinematic coverage of $2.5 < Q^2 < 6.5\,\mathrm{GeV}^2$ and $0.3 < x < 0.8$. While BETA was built with SANE's primary aim in mind—accessing deep-inelastic double spin asymmetries—the HMS also allowed two additional, single-arm measurements to be performed opportunistically during the experiment. Measurements of spin asymmetries A_1^p and A_2^p were performed by the HMS in the resonance and low-W DIS regions, and the ratio of the electric to magnetic proton elastic form factors was measured using HMS–BETA coincidences as well as HMS single-arm data.

This document describes the design of SANE, with emphasis on its non-standard additions to Jefferson Lab's Hall C, as well as the performance of each system during the experiment. We also give an overview of the analysis and corrections needed to produce spin asymmetries from BETA.

2. Polarized Electron Beam

Jefferson Lab's Continuous Electron Beam Accelerator Facility (CEBAF) consists of two linear accelerators, which at the time of this experiment, each accelerated electrons by roughly 600 MeV. Recirculating arcs connect these linacs, allowing a nominal 6 GeV maximum beam energy after 5 passes around the "race-track" [1]. Laser-excited, strained GaAs photocathodes provided a polarized electron source which switched helicity in 30 Hz pseudo-random batches. The beam current delivered to Hall C was limited to below 100 nA by the heat and radiation dose generated in the solid polarized target.

2.1. Hall C Beamline

Upon entering Hall C, the beam was expanded from below 100 μm in diameter to a $2 \times 2\,\mathrm{mm}^2$ square by two air-core magnets roughly 25 m upstream of the target, producing the "fast raster" [2]. To further retard damage to the target polarization by radiation from the beam, an additional, circular "slow raster" was created by scanning the beam over a 2.0 cm diameter spiral pattern to better cover the 2.5 cm diameter target cell [3]. Figure 1 shows each raster pattern as observed from hits in the BETA detector versus the recorded raster amplitude.

To counteract the bending of the beam down and away as it approached the target center while under the influence of the near perpendicular, 5 T magnetic field, it was passed through two dipole chicane magnets, BE and BZ, which bent the beam down and then up towards the scattering chamber, respectively. Table 1 shows the deflection of the two chicane magnets for both energy settings used while the target was in its near perpendicular configuration. Any out of plane precession of the electron spins due to the chicane transport is canceled as the beam is subsequently bent in the opposite sense by the target magnet, so the beam polarization remains unaffected.

After passing through the target, the electron beam was again deflected downwards. Rather than using a second set of chicane magnets to direct the

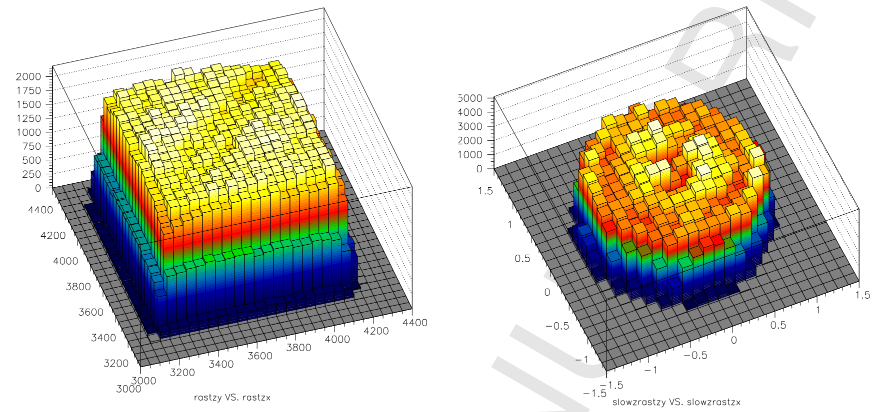

Figure 1: Magnitude of hits the detector system versus the "fast" (left) and "slow" (right) raster positions, showing the raster patterns for a typical run. At left, x and y are given in ADC channels, where 500 channels = 1 mm; at right, x and y units are in cm.

Beam E	BE Bend	BZ Bend	Target Bend
4.7 GeV	-0.878°	3.637°	-2.759°
5.9 GeV	-0.704°	2.918°	-2.214°

Table 1: Table of chicane parameters for 80° field for both beam energy settings. Negative angles indicate downward bends. The target bending angle listed is that during the approach of the beam, not the bend after the beam passes through the target center.

beam up to the beam dump, an 80-foot long helium bag was devised to transport the beam to a temporary beam dump on the experimental floor.

2.2. Beam Polarization Measurement

The beam polarization direction as it arrived in Hall C was not always 100% longitudinal due to the requirement to share polarization with the other experimental halls. The degree of longitudinal polarization was a function of both the polarization direction as the electrons left the injector, as set with a Wien filter, and the amount of spin precession through the accelerator before arrival in Hall C. The precession itself is a function of the number of passes through the accelerator, the overall beam energy, and the difference in energy between the two linear accelerators in the machine.

The beam polarization was monitored in nine dedicated Møller polarimeter measurements [4] covering each nominal beam energy and polarization setting. Periods of beam energy instability during this experiment meant that the degree of spin precession through the machine was not constant at a given energy setting, yielding more variation in the beam polarization with time than is typically expected. Therefore, the nine polarization measurements were used to interpolate the beam polarization throughout the experiment via a fit with three degrees of freedom: the intrinsic polarization of the beam at the source P_{source}, the energy imbalance of the north and south linear accelerators, and a small global correction to the overall beam energy F_{corr}. In addition, the beam polarization had been found to depend to some degree on the quantum efficiency of the photcathode, which can be described by a correction, $F(\epsilon_q)$, based on fits to data from the preceding experiment, GEp-III [5]. The beam polarization in Hall C, P_B, could then be expressed as a function of the Wien angle θ_w, quantum efficiency of the photocathode, and half wave plate status n_{hwp}, as

$$P_B = (-1)^{n_{\mathrm{hwp}}} P_{\mathrm{source}} F_{\mathrm{corr}} F(\epsilon_q) \cos(\theta_w + \varphi_{\mathrm{precession}}), \tag{1}$$

where $\varphi_{\mathrm{precession}}$ is determined by following the spin precession through each bend in the accelerator.

Using the Wien angle, beam energy, quantum efficiency and half wave plate status recorded over the course of each data-taking run, the beam polarization over time was calculated using this fit. By averaging these data over the charge accumulated on the target from beam current measurements at each moment in time, a charge-averaged beam polarization was then produced for each experimental run. For each beam energy, the Wien angle setting was chosen to maximum the combined figure of merit for polarized beam to all JLab experimental halls. At beam energy of 4.7 GeV, the Wien angle was set so that $P_B \approx P_{\mathrm{source}}$ for Hall C and P_B was not sensitive to small changes in the beam energy. Of note is the rather low beam polarization near run 72400 at the beginning of the 5.9 GeV data taking, which came from non-optimal setting of

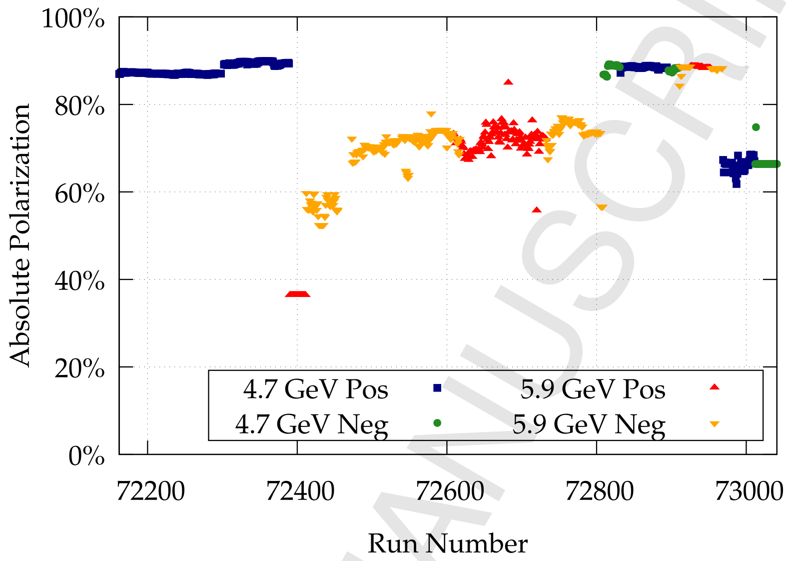

Figure 2: Electron beam polarization per data-taking run.

the Wien filter at the injector. The increase in polarization that follows results from optimizing the Wien angle. At 5.9 GeV, the Wien angle was eventually optimized so $P_B \approx 0.8 * P_{\text{source}}$, but the P_B had a small sensitivity to small changes in the beam energy which lead to the fluctuations seen in Figure 2.

3. Polarized Proton Target

SANE utilized the University of Virginia polarized solid target, which has had extensive use in electron scattering experiments at SLAC [6–8] and Jefferson Lab [9–11], and is diagrammed in Figure 3. Polarized protons were provided in the form of solid ammonia (NH_3) beads held in one of two 2.5 cm diameter, 2.5 cm long cells (*top* or *bottom*) held in the "nose" of a helium evaporation refrigerator providing roughly 1 W of cooling power at 1 K. This nose was located at the center of an Oxford Instruments NbTi, 5 T superconducting split pair magnet, which allowed beam passage parallel or perpendicular to the field. This magnet provided better than 10^{-4} field uniformity in the $3{\times}3{\times}3$ cm^3 volume of the target scattering chamber. While the magnet allowed beam passage perpendicular to the field, the geometry of the coils did occlude the acceptance of BETA when oriented at 90°, so in practice 80° was used. The field's alignment in Hall C to its nominal values were to within 0.1 degree.

Polarized target nuclei were provided via dynamic nuclear polarization (DNP) of ammonia ($^{14}NH_3$). DNP employs high magnetic fields ($B \approx 5\,\mathrm{T}$) and low temperature ($T \approx 1\,\mathrm{K}$) to align spins in a target medium, using microwave radiation to drive polarizing transitions of coupled electron–nucleus spin states [12]. These techniques offer excellent polarization of protons—exceeding 95%—in a dense solid and can maintain this polarization under significant flux of ionizing radiation, such as an electron beam.

At magnetic field B and temperature T, the polarization of an ensemble of spin ½ particles is calculable by Boltzmann statistics as $P = \tanh(\mu B/(kT))$. At 5 T and 1 K, this creates a high polarization of electron spins (99.8%), but quite low polarization in protons (0.5%). In DNP, microwave energy is used to transfer this high electron polarization to the proton spin system, which is accomplished via several mechanisms, the simplest of which to explain is the solid-state effect [13, 14]. By taking advantage of coupling between free electron and proton spins, microwave radiation of frequency lower or higher than the electron paramagnetic resonance by the proton magnetic resonance ($\nu_{\mathrm{EPR}} \pm \nu_{\mathrm{NMR}}$) drives flip-flop transitions ($e_{\downarrow}p_{\downarrow} \rightarrow e_{\uparrow}p_{\uparrow}$) to align or anti-align the proton with the field. The electron's millisecond relaxation time at 1 K means that the free electron will relax quickly to become available to perform a polarizing flip-flop with another proton. While the protons take minutes to relax, they will frequently perform energy-conserving spin flip transitions via dipole–dipole coupling with other neighboring protons. This allows the transport of nuclear polarization away from the free electron sites—a process called "spin-diffusion" which tends to equalize the polarization throughout a material [15].

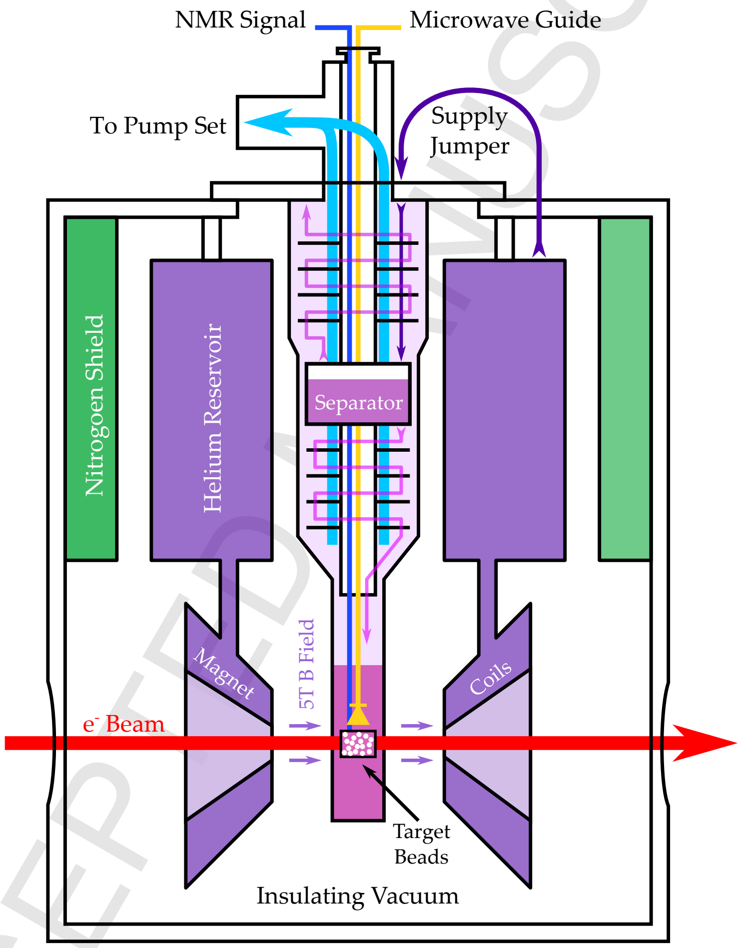

Figure 3: Cross-sectional diagram of UVa polarized target cryostat, refrigerator, and scattering chamber.

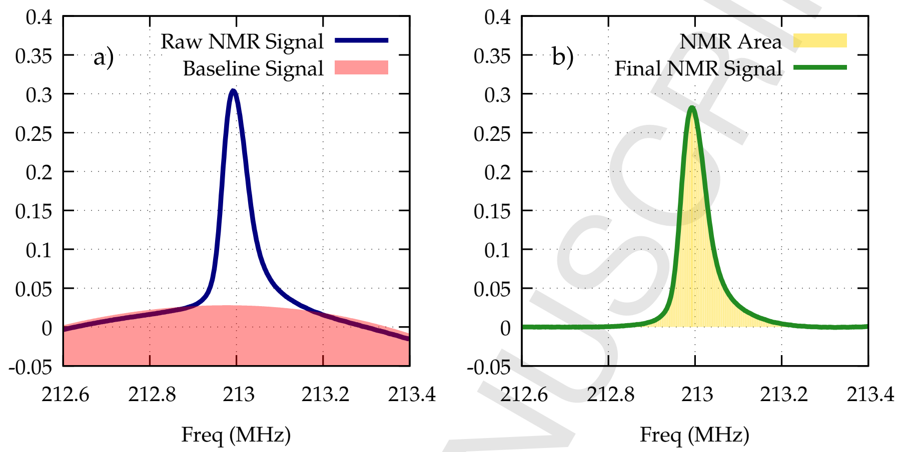

Figure 4: a) Raw NMR signal and baseline in arbitrary units. b) Final NMR signal, with baseline and residual signals subtracted, showing the integrated signal area.

3.1. Target polarization measurement

The proton polarization was measured via nuclear magnetic resonance measurements (NMR) of the target material, employing a Q-meter [16] to observe the frequency response of an LCR circuit with the inductor embedded in the target material. An RF field at the proton's Larmor frequency induces spin flips as the proton spin system absorbs or emits energy. By integrating the real portion of the response as the circuit is swept through frequency, a proportional measure of the sample's magnetic susceptibility, and thus polarization, is achieved [17].

NMR "Q-curve" signals contain the frequency response of both the material's magnetic susceptibility, and the circuits own background response. To remove the background behavior of the NMR electronics, a *baseline* signal is recorded while the proton NMR peak is shifted away from the frequency sweep range by lowering the magnetic field. To produce a final NMR signal, this baseline is subtracted, seen in a) of Figure 4, and a polynomial fit to the wings of the resulting curve is performed, allowing the subtraction of any residual background shifts in the Q-curve, as seen in b) of Figure 4. The degree of polarization is then proportional to the integrated area under this background-subtracted signal.

The coefficient of proportionality used to calculate the polarization from the integrated signal is known as the calibration constant (CC) and is determined by NMR measurements without the application of DNP. These thermal equilibrium (TE) measurements provide a signal area A_{TE} at a known polarization P_{TE}, calculable from the given field B and temperature T:

$$P_{\mathrm{TE}} = \tanh\left(\frac{\mu B}{kT}\right). \tag{2}$$

An enhanced polarization P can then be calculated from a signal area A during DNP: $P = A(P_{\mathrm{TE}}/A_{\mathrm{TE}})$. The calibration constant $P_{\mathrm{TE}}/A_{\mathrm{TE}}$ depends on the geometrical arrangement of the target material beads in the cell and the magnetic coupling of the NMR pickup coil to those beads, so in general a single constant may be applied to a target sample throughout its use in the experiment. When they were possible, multiple thermal equilibrium measurements for a given target material sample were averaged to be applied to all the target polarization data for that sample.

Figure 5 shows each calibration constant taken during the experiment, and the final averaged constants used to calibrate the NMR signal area for each target material sample. Samples number 10 and 11 have drastically different calibration constants due to the different orientation of the NMR coil to the field after the magnet was rotated; they are physically the same target samples as materials 8 and 9.

3.2. Material Preparation and Lifetime

Ammonia ($^{14}NH_3$) offers an attractive target material due to its high polarizability and radiation hardiness, as well as its favorable dilution factor — ratio of free, polarizable protons to total nucleons. Ammonia freezes at 195.5 K, and can be crushed through a metal mesh to produce beads of convenient size, allowing cooling when the material is under a liquid helium bath [18].

Before dynamic polarization is possible, the material must be doped with paramagnetic radicals, which provide the necessary free electron spins through-

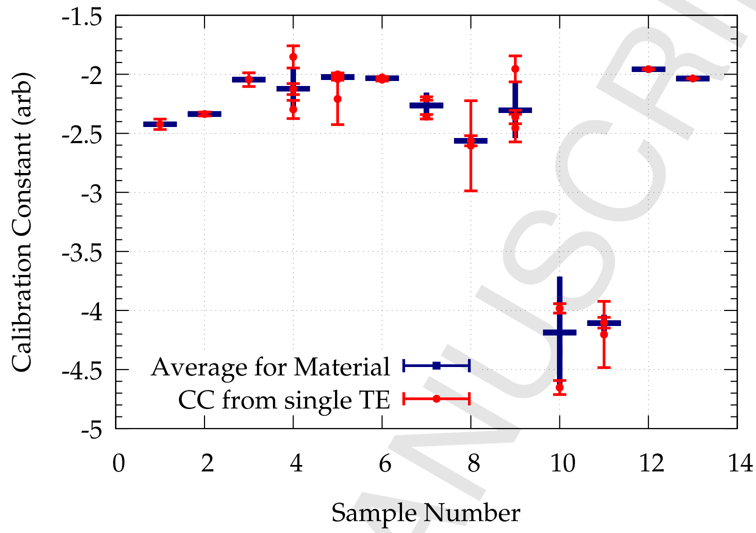

Figure 5: Calibration constants for each target material sample used during the experiment. The calibration constant used to calculate the final target polarization is an average of one or more values from all the thermal equilibrium measurements taken for that sample. Errors shown are statistical only.

out the material. For SANE, the ammonia target samples were radiation doped at a small electron accelerator, the Medical-Industrial Radiation Facility at NIST's Gaithersburg campus. Free radicals were created by 19 MeV electrons at a beam current between 10 and 15 μA, which was incident upon the frozen ammonia material held in a 87 K liquid Ar_2 bath, until an approximate dose of $100\,\mathrm{Pe/cm^2}$ was achieved. In this context, a unit of radiation dose of $1\,\mathrm{Pe/cm^2} = 10^{15}\ \mathrm{e^-/cm^2}$ is convenient.

While proton polarizations exceeding 95% are possible after irradiation doping of ammonia, the experimental beam causes depolarization. The first depolarizing effect, of order 5%, is due to the decrease in DNP efficiency due to excess heat from the beam [19]. A longer term depolarization effect comes from the build up of excess radicals under the increasing dose of ionizing radiation. These excess radicals mean more free electrons which provide more paths for proton relaxation and depolarization.

By heating the target material to between 70 and 100 K, certain free radi-

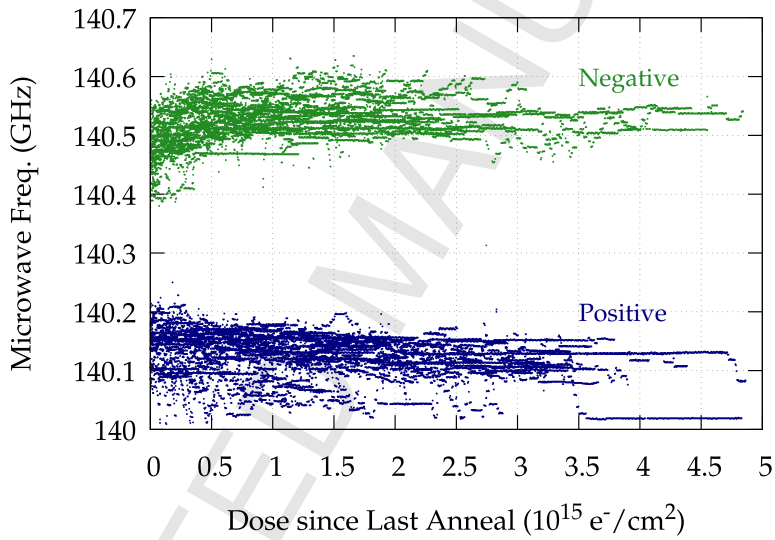

Figure 6: The change in microwave frequency used to polarize during SANE as radiation dose from the beam is accumulated. Positive polarization points (below 140.3 GHz) show a roughly linear decrease, while the negative polarization points (above 140.3 GHz) exhibit a curving increase.

cals can be recombined. This *anneal* process will often allow the polarization to achieve its previous maximal values. With subsequent anneals, however, the build-up of other radicals with higher recombination temperatures will result in an increased decay rate of the polarization, until the material must be replaced [20].

While the maximum achievable polarization falls as continued radiation dose is accumulated, the optimal microwave frequency needed to reach the highest polarization will also shift as the free electrons come under the dipole–dipole influence of more free electron neighbors, broadening the electron spin resonance peak. Figure 6 shows the shift in microwave frequency chosen by the target operator during the experiment, as a function of the dose accumulated on the target since the last anneal.

Figure 7 shows the lifetime of a typical target material used during SANE, and illustrates several artifacts common during beam taking conditions. Vertical yellow lines depict anneals. The build-up of radicals in beam can be seen at 0 and $6\,\mathrm{Pe/cm^2}$ as polarization actually increases with dose accumulated. Small spikes in polarization seen throughout are the result of beam trips, when the polarization improves as the temperature drops with the loss of heat from the beam. Other hiccups in operation apparent in the plot are a poorly performed anneal, just after $2\,\mathrm{Pe/cm^2}$, resulted in starting polarization below 60%, and the loss of liquid helium in the target cell at approximately 3 and $11\,\mathrm{Pe/cm^2}$.

3.3. Offline Corrections

Several corrections were necessary to the online NMR signal analysis that was performed as the experiment ran. Because the scale of the thermal equilibrium signals is two orders of magnitude smaller than that of the enhanced polarization signal, different amplification gains are used for the two measurements. Differences between the nominal and actual gains of the amplifiers result in a correction of approximately 1%.

During the running of the experiment, the superconducting magnet experienced a damaging quench which necessitated repairs. While 5 T operation of the

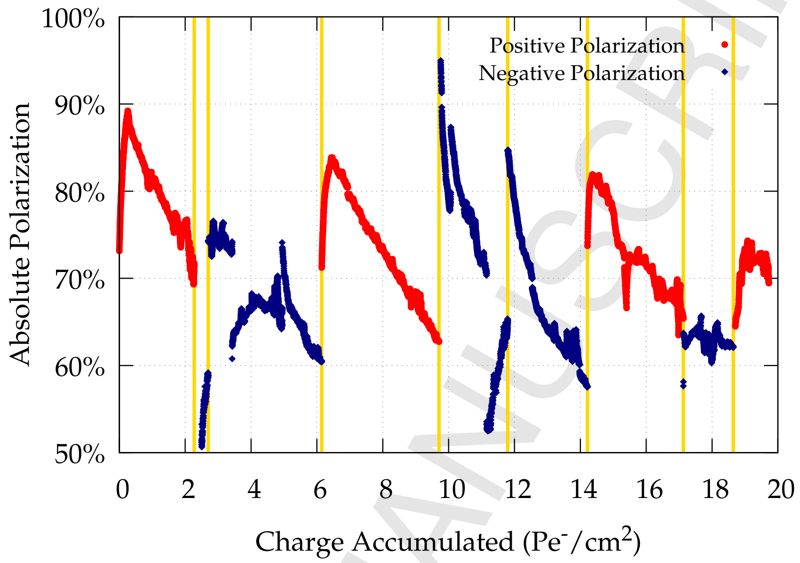

Figure 7: Polarization of a typical target material sample versus charge accumulated during data taking, with vertical yellow lines showing when anneals were performed.

magnet was restored, a slight current leak while in persistent mode was seen due to minute electrical resistance [21]. While the change in magnet current was only about 0.05% per day, this resulted in a significant shift in the NMR signal peak. The wings of each signal—after baseline subtraction— are used to perform a polynomial fit to remove residual Q-curve movement, so the shifting peak created poor fits as it approached the edge of the sweep range. This effect was corrected by varying the size of the wings used in the polynomial fit for each signal, ensuring that only the background portion of the signal was included in the fit.

3.3.1. Target Polarization Performance

During SANE, a total of 122.2 Pe/cm^2 of radiation dose was accumulated on the 11 different ammonia material samples. Anneals were performed 26 times, and 23 thermal equilibrium calibration measurements were taken. Figure 8 shows the polarization for each experimental run, with indications for the orientation of the target during that period. Despite considerable unforeseeable

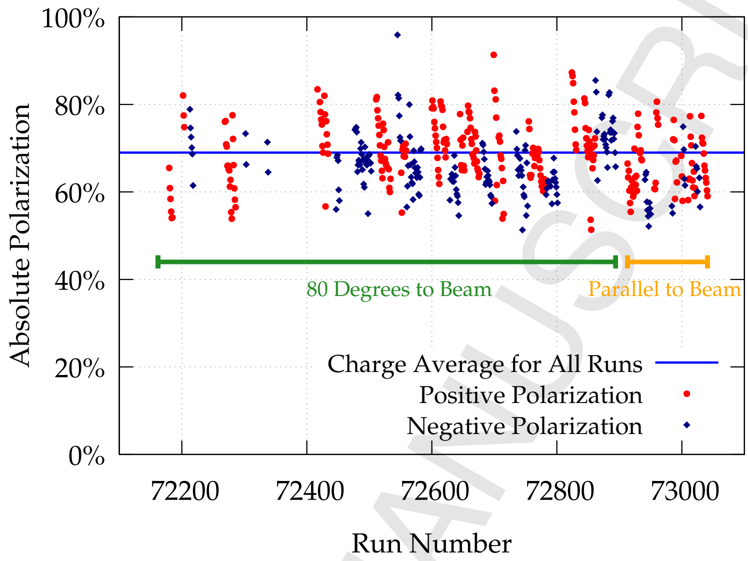

Figure 8: Charge averaged target polarization achieved for each SANE data-taking run.

difficulties in the operation of the target during SANE, the total charge-averaged proton polarization achieved was 68%.

4. Detector Systems

The centerpiece of SANE's inclusive measurement of deep inelastic electron scattering was the Big Electron Telescope Array (*BETA*)[1], a large acceptance, non-magnetic detector package situated just outside the target vacuum chamber (see Figure 9). Electrons scattered in the target passed though a small tracking hodoscope for position information, a threshold Cherenkov detector for electron discrimination, and a second, large hodoscope, before finally producing a shower in the calorimeter. BETA occupied a large, 0.2 sr solid angle at 40° to the beam direction, and provided pion rejection of 1000:1, energy resolution of better than $10\%/\sqrt{E}$, and angular resolution of approximately 1 mr. Figure 10 shows renderings of a Geant4 simulation of BETA with an example electron track.

[1]The original BETA design was conceived by Glen Warren [22].

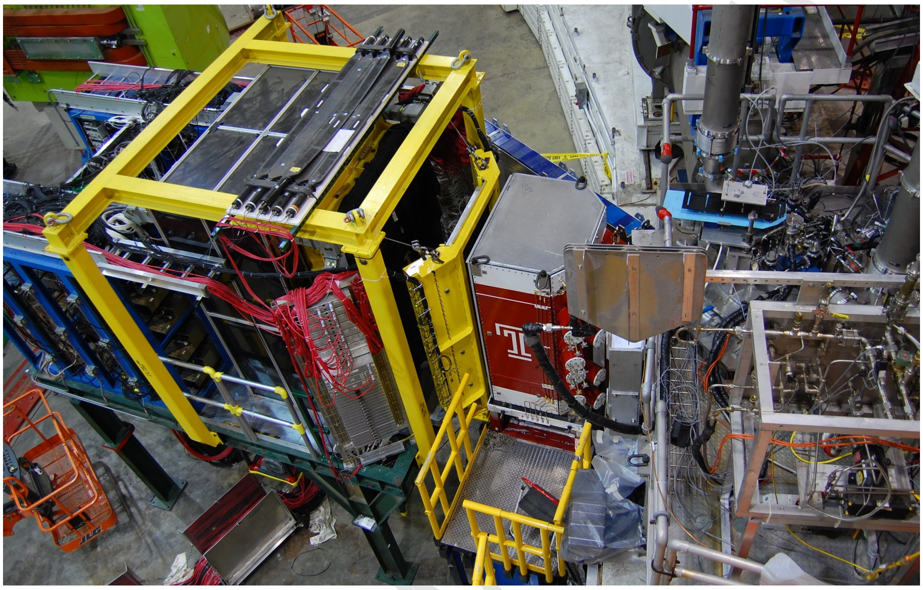

Figure 9: Photograph of BETA from above, showing the support structure for the calorimeter at left, lucite hodoscope in yellow at center, Cherenkov tank in red, and target platform at right.

4.1. BigCal

BETA's big electromagnetic calorimeter, *BigCal*, consisted of 1,744 TF1-0 lead-glass blocks; 1,024 of these were $3.8 \times 3.8 \times 45.0$ cm^3 blocks contributed by the Institute for High Energy Physics in Protvino, Russia. The remaining 720, from Yerevan Physics Institute, were $4.0 \times 4.0 \times 40.0$ cm^3 and were previously used on the RCS experiment [23]. The calorimeter was assembled and first utilized by the GEp-III collaboration [24]. The Protvino blocks were stacked 32 $\times$ 32 to form the bottom section of BigCal, and the RCS blocks were stacked 30 $\times$ 24 on top of these, as seen in Figure 11. The assembled calorimeter had an area of roughly 122×218 cm^2, which, placed 335 cm from the target cell, made a large solid angle of approximately 0.2 sr at a central scattering angle of 40°.

BigCal was the primary source for event triggers for BETA, and a summation scheme was used to simplify triggers and reduce background events, summarized

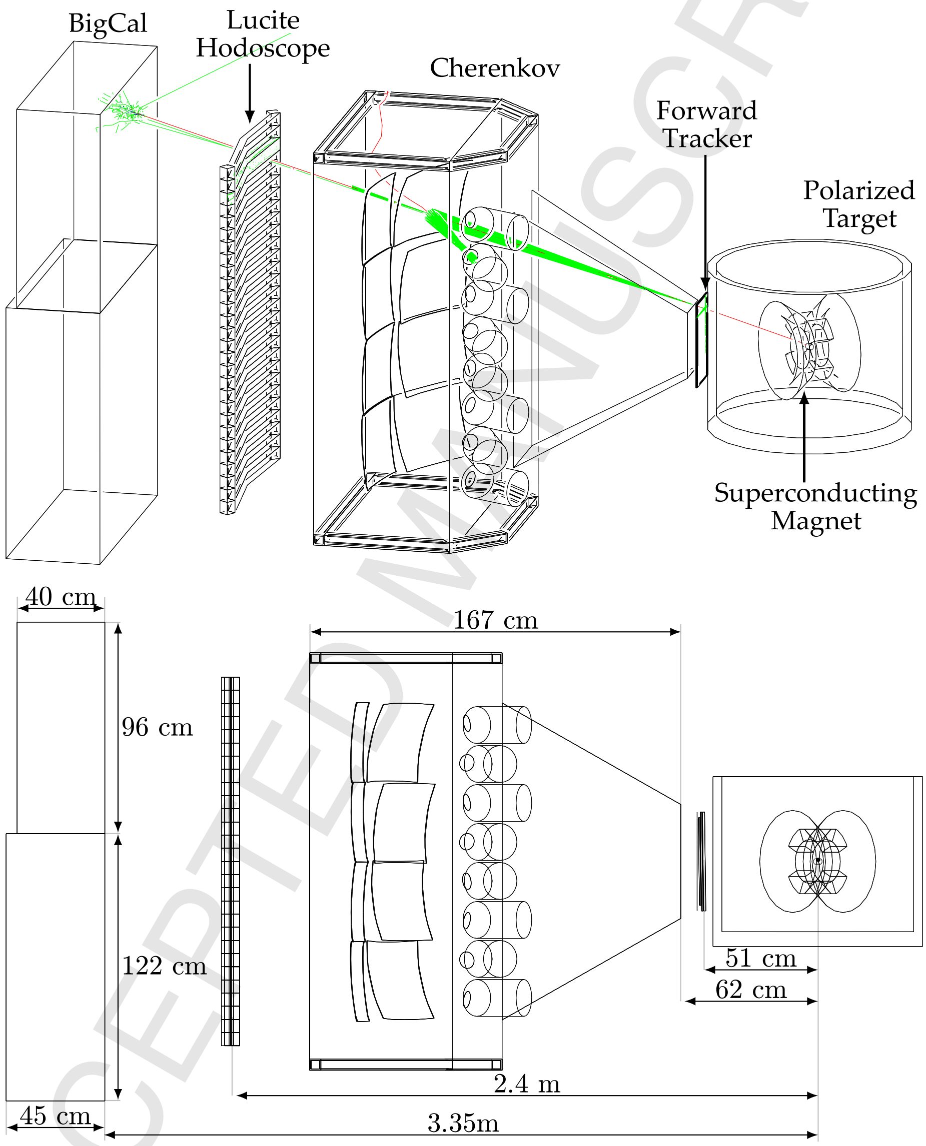

Figure 10: Two renderings of BETA from the Geant4 simulation, showing at top a simulated electron event originating in the target, creating Cherenkov showers in the gas Cherenkov and lucite hodoscope, and depositing its energy in the upper section of the calorimeter. The lower diagram shows the dimensions of each components, and their distances from the target.

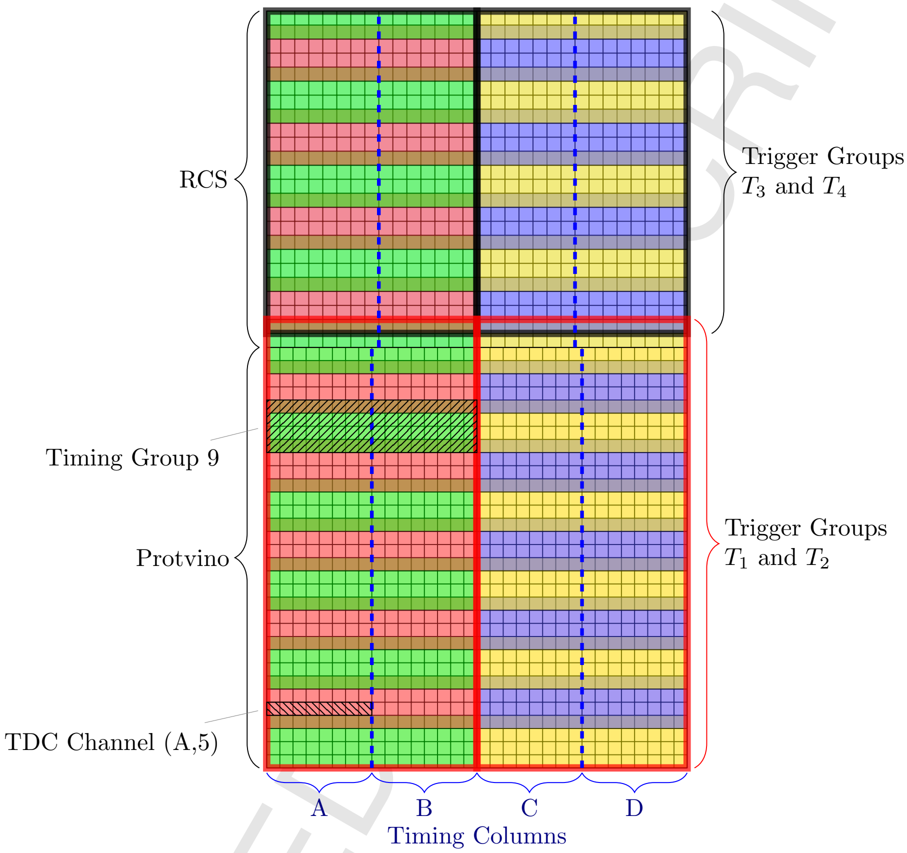

Figure 11: Layout of BigCal's 1,744 lead-glass blocks, showing upper RCS and lower Protvino sections, as well as trigger and timing groups. An example 8 block TDC channel and 64 block timing group are show in hatched areas [25].

in Figure 11. While each lead-glass block had its own FEU-84 photomultiplier tube and ADC readout, the smallest TDC readouts consisted of groups of 8 blocks in one row. These TDC groups then formed 4 timing columns, which were summed and discriminated for another TDC readout. The 8 block TDC signals were also summed into larger timing groups of 64 blocks, 4 rows by 8 columns (designated by color in Figure 11), which were overlapped to avoid split events. Finally, timing groups were summed into four trigger groups to form the main DAQ triggers [24].

4.2. Gas Cherenkov

The Cherenkov counter held dry N_2 radiator gas at near atmospheric pressure, and employed eight 40×40 cm^2 mirrors to focus Cherenkov photons onto 3 inch diameter Photonis XP4318B photomultiplier tubes. Nitrogen's index of refraction of 1.000279 gave a momentum threshold for Cherenkov emission by pions of 5.9 GeV/c, allowing effective rejection of pions, given a maximum beam energy of 5.9 GeV. The 8 mirrors, 4 spherical and 4 toroidal, were positioned to cover the full face of BigCal, effectively dividing BigCal into 8 geometric sectors each corresponding to one mirror. Due to the proximity of the Cherenkov tank to the target magnetic field, μ-metal shields enclosed each photomultiplier tube, and additional iron plating was situated between the tank and magnet. The design and performance of the SANE Cherenkov is discussed in detail in reference [26].

4.3. Hodoscopes

Two tracking hodoscopes provided additional position information and background rejection. Mounted between BigCal and the Cherenkov tank, the lucite hodoscope consisted of 28 lucite bars of $3.5 \times 6.0 \times 80.0$ cm, curved with a radius equal to the distance from the target cell, giving a normal incidence for participles originating in the target. With an index of refraction of 1.49, Cherenkov radiation was produced from the passage of charged particles above $\beta_{\text{threshold}} = 0.67$. The effective threshold increases to 0.93 when Cherenkov photons are detected simultaneously at both ends of the lucite bar, because these photons propagate through total internal reflection. The Cherenkov angle must be above critical angle for lucite (42°) in this case. Photonis XP2268 photomultiplier tubes coupled to the end of each bar collected the Cherenkov light, allowing the determination of the position of the hit along the bar using timing information from both tubes.

A smaller, front tracking hodoscope consisted of three planes of 3×3 mm Bicron BC-408 plastic scintillator bars positioned just outside the target scattering chamber, 48 cm from the target cell. This hodoscope provided tracking information on particles as they were still under the influence of the target's magnetic field. By combining tracking information close to the target with final positions in BigCal, any discernible curve in the particles trajectory would allow differentiation of positively and negatively charged particles, allowing positron rejection.

4.4. Hall C HMS

The standard detector system in Hall C, the High Momentum Spectrometer (HMS), was utilized in a supporting role throughout the experiment. The HMS is made up of three superconducting quadrupole magnets and one superconducting dipole, which focus and bend charged particles into a detector package with two gas drift chambers, four hodoscopes, a gas Chereknov tank and a lead-glass calorimeter. During SANE, the HMS was positioned at 15.4°, 16.0° and 20.2°, accepting proton and electron scattering events from the target. In addition to the calibration and support of BETA, events from the HMS were used to produce independent analyses on the proton electric to magnetic form factor ratio [27] and spin asymmetries and structure functions [28].

4.5. Data Acquisition

Data collection was coordinated by a trigger supervisor [29], which received triggers from BigCal, Cherenkov and HMS TDCs. If not busy, the trigger supervisor accepted triggers from readout controllers, sending gate signals to ADCs and start signals to TDCs. Readout controllers then read out signals, to be assembled by an event builder and saved to disk. To monitor events missed due to the data acquisition being in a busy state, the dead-time was monitored with scalers on the discriminator output which wrote to the data stream every 2 seconds.

SANE utilized 8 trigger types, representing triggers and coincidences from the detectors, of which 2 were used in the final analysis. The `BETA2` triggers were the result of coincident hits in the Cherenkov and BigCal, representing a candidate electron event. `PI0` triggers required two BigCal hits in different quadrants of the detector, representing two, vertically-separated photon events from neutral pions.

5. BETA Commissioning and Calibration

SANE's initial commissioning and calibration schedule was interrupted by an unanticipated target magnet failure and subsequent repairs. The delays meant the cancellation of plans to calibrate BigCal with elastic *e*-*p* scattering using coincidences with protons detected in the HMS. In this scheme, the target magnet strength and orientation would have been varied to scan the elastic events across the full face of the calorimeter while running at reduced beam energy. In order to optimize data collection for the proposed beam energy and target configurations while accommodating the accelerator run plan, the commissioning of the BETA detectors began with transverse target magnet orientation rather than parallel. In total, the target magnet failure and unrelated accelerator operation issues contributed to roughly 45% fewer data being collected than was originally proposed.

Instead, BETA's BigCal calorimeter was calibrated in real-time using neutral pion events from the target, allowing drifts in gain to be observed throughout the experiment. The Cherenkov photomultiplier tube ADC channels were calibrated before the experiment to roughly 100 channels per photo-electron, as discussed in detail in reference [26]. The Lucite hodoscope was used only for TDC data to record the position of hits, calculable from propagation of the electron's Cherenkov light to photomultiplier tubes at each end of the bar.

5.1. Cluster Identification

To reconstruct the final energy and position of particle hits in the calorimeter, a simple algorithm was used to group signals originating from one shower in neighboring calorimeter blocks into clusters for each event. The block with the largest signal was selected as the cluster seed, and struck blocks within a 5×5 grid of this centroid were included in the cluster, unless detached from the group. The next cluster was formed by finding the next highest signal block, excluding those already included in a cluster, and this process was repeated until all blocks above a chosen threshold were used.

Once clusters were identified, they were characterized for use in the analysis. We assigned each cluster a pre-calibration energy $E_c = \sum_i c_i A_i$ for block number i, ADC values A_i and block calibration constants c_i, where final c_i are the end goal of the calibration. In the first pass of analysis, each ADC channel was assumed to be 1 MeV, based on adjustments before the experiment using cosmic ray events. The moment of the cluster is then an energy weighted average of position

$$\langle x \rangle = \sum_i \frac{c_i A_i}{E_c}(x_i - x_{\text{seed}}), \quad (3)$$

and similarly for $\langle y \rangle$, so that the cluster position on the face of BigCal was taken to be $(x_{\text{seed}} + \langle x \rangle, y_{\text{seed}} + \langle y \rangle)$. The second moment gave the position standard deviation.

5.2. π^0 Calibration

The large number of π^0 background events incident on the calorimeter from the target allowed reliable calibration of a majority of the calorimeter, as well as effective, real-time gain monitoring throughout the experiment. Neutral pions produced in the target decay to two photons at a 98.8% branching probability with a mean lifetime of 8×10^{-17} seconds, so that most pions have decayed to photons before exiting the target. By measuring the separation angle of the photons α, we can determine the relative energies of the incident photons $E_{1,2}$ from the pion mass $m^2_{\pi^0} = 2E_1E_2(1 - \cos\alpha)$.

Unfortunately, the `PI0` trigger was unable to populate all calorimeter blocks with events because the trigger required two of the four trigger groups to fire in coincidence (T_{1-4} shown in Figure 11). The reach of the events was limited by the energy thresholds for each trigger groups' discriminator, which was set to roughly 400 MeV. For example, to populate the upper-left most block with a photon shower requires relatively low energy π^0 decays, so that the angle between the two photons is large enough to trigger T_3 and T_4. If the π^0 is too energetic, the angle isn't big enough to reach both trigger groups. In hindsight, the solution would have been to use smaller trigger groups to form the PI0 trigger.

To supplement the π^0 calibration and improve the energy calibration of blocks at the edges of the calorimeter, a calibration was done by looking at the energy spectra measured in each block. A GEANT simulation of the experiment was run with events weighted by the inelastic cross section [30]. The energy spectra for each block is dominated by inelastic electrons in the high energy tail. The energy gain coefficients for a block were set so that the measured energy spectra for each block matched the GEANT simluated energy spectra in the high energy tail region for $W < 2.0\,\text{GeV}$. These energy gain coefficients were used as the starting values for determining the final gain coefficients in the π^0 calibration method.

Events from the PI0 trigger were chosen and cuts were placed to include only clusters which were 20 cm to 80 cm apart, excluding pairs produced outside the target, and to exclude events that gave triggers in the Cherenkov, such as electrons. To calibrate a given block, a histogram of the invariant mass results was formed for all the clusters which passed the cut and included that block. Normalizing this invariant mass result to the known pion mass $\pi^0 = 134.9\,\text{MeV}$, a new calibration constant was obtained for the block. Once new constants were produced for all blocks, this process was repeated and iterated many times until all block results converged on the pion mass, as seen in Figure 12.

Simultaneous with the collection of BETA's main inclusive e data, e-p elastic coincidence data was taken employing the HMS to gather the proton's momentum and angle. Using the known beam energy and the measured proton momentum in the HMS, the scattered electron energy can be calculated (EHMS), giving the only explicit measure of the calorimeter energy resolution for electrons. The acceptance-averaged value of the electron momentum was 2.0 and 2.6 GeV for beam energies of 4.7 and 5.9 GeV. The difference between EHMS and the energy measured in the calorimeter (ECalo) is plotted in Figure 13 for the beam energies of 4.7 (a) and 5.9 GeV (b); Gaussian fits show energy resolutions of 9.1 ± 0.5% and 9.08 ± 0.03% in each case.

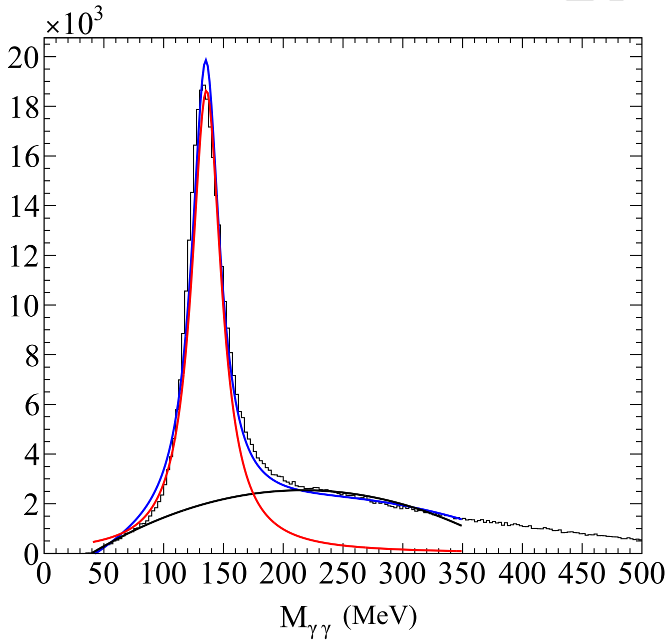

Figure 12: Plot of neutral pion mass reconstruction after block calibration. The energy resolution of this peak is directly proportional to the energy resolution of the clusters in the calorimeter.

5.3. Neural Networks and Track Reconstruction

Three neural networks were constructed to aid the track reconstruction for BETA: (a) a BigCal position correction network, which determined the x–y coordinate where the a photon track crossed the calorimeter face; (b) a second network for the x–y coordinate correction for charged particles, necessitated by the difference between the shower profiles of electrons and positrons, and photons; and (c) a network to determine the scattered momentum vector at the target, correcting for the deflection of charged tracks as they propagated through the target magnetic field. Each neural network was trained for each particle type (electron, positron, and photon) and target field/beam energy configuration. A Geant4 simulation with a detailed description of the geometry and an extended target field map was used to generate the events for training each neural network. Roughly 1 million events were simulated with uniformly distributed angle and energy, and originating uniformly from the target volume.

5.3.1. Photon Position Corrections

Particles incident on the calorimeter farther away from the center of its face arrived at more oblique angles to the surface, so that the depth of the shower had an increasing effect on the resolved cluster moment. Photons hitting the calorimeter at the top or bottom enter the face of the calorimeter at angles far from normal incidence. Therefore the electromagnetic shower's longitudinal development will have the same directional bias. The x and y moments for these types will result in a shift that depends on the incident angle (which for photons is easily mapped to its position). In order to correct for this, a neural network (a) was trained to provide the reconstructed x-y coordinates of where the photon crossed the face of the calorimeter. The neural network provided the correction values $\delta_x = x_{\mathrm{face}} - x_{\mathrm{cluster}}$ and $\delta_y = y_{\mathrm{face}} - y_{\mathrm{cluster}}$, the difference between the position on the face of BigCal where the particle entered and centroid of the cluster created in BigCal.

This photon position correction neural network (a) followed the Broyden-Fletcher–Goldfarb–Shanno (BFGS) training method [31], using a sigmoid activation for all nodes. Quantities characterizing the cluster, such as its mean position, standard deviation, skewness and kurtosis, were used as input neurons. The strongest neuron weights for the δ_y correction were connected to the y position input neuron, so that with increasing distance from the calorimeter center, the correction for the oblique angle of incidence increased, as well. Figure 14 shows the performance of the neural network for the y position correction.

5.3.2. Electron Reconstruction

Using the hits in BETA and knowledge of the target's 5 T field, the trajectory of the scattered electron was reconstructed to allow the determination the kinematics of each event. While naïve, straight-line tracks from x and y calorimeter hits to the target gave initial physics scattering angles θ and ϕ, corrections were made to take into account the angle of incidence in the calorimeter and, more importantly, the bending of the electron in the magnetic field. The electron and positron x-y position correction neutral network (b) was very similar to the network for photons, shown in Figure 14. The final neural network (c) was trained to produce the physics scattering angles θ and ϕ. Figure 15 shows the network performance for the physics scattering angle θ.

5.4. Cherenkov Calibration

Each of the Cherenkov's eight ADC spectra were normalized to their average single-electron track signal, which corresponded to roughly 18 photoelectrons. This provided an ADC spectrum calibrated to the number of electrons and positrons, as seen in Figure 16, which shows a fit for the relative contribution of single and double tracks. These "double tracks" are electron–positron pairs produced outside the target field—either in the scattering window, front hodoscope, or Cherenkov window— that travel co-linearly after production to create a single cluster in the calorimeter. Pairs produced in the target separate due to the field, to be rejected as two-cluster events if both arrived in the calorimeter, or remain as background if only one arrived in the calorimeter (see section 6.2.6). The single and double track signal fit results were used to estimate the double track background in an ADC window cut (see section 6.1).

6. Asymmetry Analysis

Because BETA was a new detector configuration, we discuss here the analysis framework required for its inclusive spin asymmetry measurements, leaving HMS analysis details to other works [32, 33]. Deep-inelastic scattering electron events detected in BETA were reconstructed, separated into kinematic bins, formed into yields based on the beam helicity, and corrected to produce physics asymmetries at each target field angle. These asymmetries take the form

$$A = \frac{1}{fP_BP_T}\frac{N_+ - N_-}{N_+ + N_-}, \tag{4}$$

for dilution factor f, beam and target polarizations P_B and P_T, and corrected electron yields for each beam helicity $N_{\pm}$. Here the target and beam polarizations are applied as a single, charge averaged value for all events in each experimental run, while the dilution factor and the yields are functions of the kinematics of each event.

6.1. Event Selection

To minimize backgrounds and ensure that good electron events were counted in the yields, events were rejected if they did not meet the following criteria. For asymmetry yields, only single cluster events in BigCal with a corresponding Cherenkov hit were taken. A cut was placed on the Cherenkov hit geometry, ensuring that the position in the calorimeter matched a hit in the correct Cherenkov sector. To reduce the systematic error due to the π^0 background subtraction (described in section 6.2.6), single clusters in BigCal below an energy cut of 900 MeV were excluded. The Cherenkov window cut provided a clean selection of single-track events and removed most of the background contribution from double-track events. The dominant source of double-track events came from pair production outside of the strong target magnetic field. The Cherenkov ADC window cut is shown in Figure 17.

6.2. Asymmetry Measurements

To extract physics spin asymmetries, SANE directly measured double-spin asymmetries with the target's magnetic field anti-parallel and at 80° to the beam. Reconstructed electron event yields from each helicity $n_{\pm}$ were used to form raw asymmetries A_{180° and A_{80°, as a function of their x and Q^2 kinematic bins:

$$A_{\text{raw}}(x, Q^2) = \frac{n_+(x, Q^2) - n_-(x, Q^2)}{n_+(x, Q^2) + n_-(x, Q^2)}. \tag{5}$$

These raw asymmetries must be first corrected for the effects of dead time in the data acquisition system, unequal total electron events in each helicity, and the dilution of the target by material other than the protons of interest.

6.2.1. Charge Normalization and Live Time Correction

Although the 30 Hz, pseudo-random helicity flips of the beam produced nearly equal number of positive and negative helicity incident electrons, any imbalance in the beam charge between the two helicity states would introduce a false asymmetry. This effect was corrected by normalizing the asymmetry using total charge accumulated Q_+ and Q_- from each helicity. The beam charge was measured by a cylindrical cavity which resonates at the same frequency as the accelerator RF in the transverse magnetic mode as the beam passes through the cavity. The RF power of the resonance was converted by antennae in the cavity into an analog voltage signal. This analog signal was processed into a frequency which was then counted by scalers which were gated for beam helicity. A special set of data was taken to calibrate the beam current measured in the hall relative to the beam current measured by a Faraday cup in the accelerator injector at various beam currents. The scalers were injected into the datastream every two seconds, and experimental data was used only if the beam current was between 65 and 100 nA.

Typically, scalers measured the total number of accepted triggers, $n_{\pm}^{\rm acc}$, and the total trigger events, $n_{\pm}^{\rm trig}$, for each helicity. To account for the computer livetime from either helicity due to event triggers that arrived while the data acquisition was busy, the corrected yield was divided by the computer livetime: $L_{\pm} = n_{\pm}^{\rm acc}/n_{\pm}^{\rm trig}$. Together, the charge normalization and livetime corrections resulted in corrected yields

$$N_{\pm} = \frac{n_{\pm}}{Q_{\pm}L_{\pm}}, \tag{6}$$

for raw counts $n_{\pm}$ of electron yields of each helicity, for each run, and as a function of kinematic bin.

Unfortunately, during SANE the total positive beam helicity trigger events from the scalers was not measured and therefore a direct measure of L_+ was not made. The total negative beam helicity trigger events were, however, recorded by the scalers, as were the accepted trigger events for both helicities. The livetime for the negative helicity was calculated for each run from the scaler data.

Given the trigger rates of the experiment, the livetime could be approximated as $1-\tau R^{\text{trig}}$, where R^{trig} is the rate of triggers and τ is the computer deadtime of the data acquisition system. For each run, τ was determined from the negative helicity data and the livetime for each helicity, $L_{\pm}$, was calculated as $1-\tau R_{\pm}^{\text{trig}}$. A plot of the livetime for the negative helicity events for all the runs in the experiment is shown in Figure 18. For most of the experimental data, the livetime measurement was consistent with $\tau \approx 160$ μsec. However, the 4.7 GeV, perpendicular-target data shows large variations in the livetime with only small variation in trigger rate, implying that τ must have been fluctuating. The cause of this effect is not fully understood.

To check the effectiveness of the charge and livetime corrections to the data, a measurement of the false asymmetry was done using the trigger asymmetry, $A_{p,n}$, as measured with positive (p) or negative (n) combinations of beam, P_B, and target, P_T polarizations. The false asymmetry was calculated as

$$A_{\text{false}} = \frac{C_p A_n - C_n A_p}{C_p - C_n}, \tag{7}$$

and $C = P_B P_T$, with the $p(n)$ indicating the sign of C. In Figure 19, the false asymmetry is plotted as a function of run number.

6.2.2. Packing Fraction

The ammonia target samples consisted of irregular beads roughly 2 mm in diameter, cooled in a liquid helium bath and held with aluminum foil windows. Each sample differed slightly in the amount, size and shape of the beads used. To determine what portion of the target cell was ammonia, called the packing fraction p_f, experimental yields from the HMS were compared to simulation. A carbon disk target was utilized in specialized runs throughout the experiment to provide yields with a well-known cross section and density, giving a normalization for the HMS acceptance and beam charge. The electron yield was a linear function of the packing fraction $Y(p_f) = mp_f + b$, where m and b depend on the beam current, acceptance, partial densities and cross sections.

Using this linear relation, the packing fraction of a given sample was determined by interpolating between two reference points on the line, as simulated from a Monte Carlo. The Hall C HMS single arm Monte Carlo—based on an empirical fit of inelastic cross section [30, 34] and containing realistic HMS, target and field geometries—was run with target packing fraction set to 50%, and again with packing fraction set to 60%. The simulated yields from these two points of known packing fraction provided the necessary line for interpolating the target sample's packing fraction from the given HMS experimental yields. Figure 20 shows the calculated packing fractions for all SANE target material samples.

6.2.3. Dilution Factor

The dilution factor, f, is a kinematics dependent correction to the measured asymmetries to account for contributions of unpolarized nucleons in the target. Essentially a ratio of the cross-sections of the polarized protons to the nucleons of all other materials in the target cell, the dilution factor was calculated for each experimental run as

$$f(W, Q^2) = \frac{N_1\sigma_1}{N_1\sigma_1 + N_{14}\sigma_{14} + \Sigma N_A\sigma_A}, \tag{8}$$

for number densities N_A of each nuclear species present in the target of atomic mass number A, and radiated, polarized cross-sections $\sigma_A(W, Q^2)$ [35]. This factor covers not only the protons (1) and nitrogen (14) in the ammonia sample, but must also include other materials such as helium (4) and aluminum (27). Substituting numeric values for this specific target, the dilution factor is expressed in terms of these cross sections and the packing fraction p_f as

$$f = \left(1 + \frac{\sigma_{14}}{3\sigma_1} + 0.710\left[\frac{4}{3p_f} - 1\right]\frac{\sigma_4}{3\sigma_1} + \frac{0.022}{p_f}\frac{\sigma_{27}}{3\sigma_1}\right)^{-1}. \tag{9}$$

Cross sections for each species needed for Equation 9 were calculated from empirical fits to structure functions and form factors, and included all radiative corrections used later in the analysis. The dilution factor for a typical run is shown in Figure 21 in x bins.

6.2.4. Target Radiation Thicknesses

The thickness of each radiator in the scattering chamber was required for the calculation of external radiative corrections. Table 2 shows the radiation thickness for all materials traversed by the beam passing through the target, for a nominal packing fraction of 0.6, as well as the percentage of radiation length χ_0.

Component	Material	Thickness (mg/cm^2)	χ_0 (%)
Target Material	$^{14}NH_3$	1561	3.82
Target Cryogen	LHe	174	0.18
Target Coil	Cu	13	0.10
Cell Lid	Al	10	0.04
Tail Window	Al	27	0.12
Rad Shield	Al	7	0.03
N Shield	Al	10	0.04
Beam Exit	Be	24	0.04
Vacuum Windows	Be	94	0.14
	Al	139	0.58
	80° Total, Before Center		2.98
	80° Total, After Center		2.36
	180° Total, Before Center		2.54
	180° Total, After Center		2.36

Table 2: Table of target component thicknesses for radiative corrections. Total thicknesses before and after the center of the target are given for each magnet orientation configuration.

6.2.5. Polarized Nitrogen Correction

While the dilution factor correction accounts for scattering from material other than protons, it does not take into account the effect of any polarization of such material in the asymmetry. Nitrogen, in particular, provides a third of the polarizable nucleons in ammonia. During usual DNP conditions, the polarization of the spin-1/2 protons (P_p) and spin-1 nitrogen (P_N) in $^{14}NH_3$ are related as

$$P_N = \frac{4\tanh((\omega_N/\omega_p)\,\mathrm{arctanh}(P_p))}{3+\tanh^2((\omega_N/\omega_p)\,\mathrm{arctanh}(P_p))}, \tag{10}$$

where ω_N and ω_p are the ^{14}N and proton Larmor frequencies [36]. At maximum proton polarizations of 95%, the nitrogen polarization will be only 17%. In addition, in nitrogen a nucleon's spin is aligned anti-parallel to the spin of the nucleus one third of the time [37]. These effects together result in a maximum polarization of anti-parallel nitrogen nucleons of roughly 2%, which results in an added systematic error to the asymmetries of less than half a percent.

6.2.6. Pair-symmetric background subtraction

At lower scattered electron energies, the pair-symmetric background becomes significant, and pair conversions that happen in, or very near, the target cannot be completed rejected. Cherenkov window cut (shown in Figure 17) was only capable of removing double-track events—tracks which produce twice the amount of Cherenkov light as a single electron track. Double-track events are the result of e^+–e^- pairs which are produced outside of the target. These are not significantly deflected by the magnetic field, and thus appear as one cluster with twice the expected Cherenkov light, easily removed by the Cherenkov window cut. However, pairs produced in the target material are significantly deflected, causing only one particle to be detected in BETA. These events can not be removed with selection cuts and are misidentified as DIS electrons.

To compensate for the pair-symmetric background, the scattering asymmetry A from Equation 4 was corrected with

$$A_{\mathrm{corrected}} = A/f_{\mathrm{BG}} - C_{\mathrm{BG}}. \tag{11}$$

where f_{BG} is the background dilution, and C_{BG} is the pair-symmetric background contamination of the measured asymmetry. The background dilution term corrects for the unpolarized background contribution to the total yield, and the contamination term removes any background asymmetry contributing to the measured asymmetry.

The dominant source of pair-symmetric background events came from conversion of $\pi^0 \to \gamma\gamma$ decay photons. Events passing the selection cuts were either inclusive electron scattering events or pair-symmetric background events. The background dilution is then $f_{\rm BG} = 1 - f_{\rm SANE}$, where $f_{\rm SANE} = n_{\rm BG}/n_{\rm total}$ is the ratio of background to total scattering events. The contamination term is defined as

$$C_{\rm BG} = \frac{f^p_{\pi^0}}{f} \frac{A_{\pi^0} f_{\rm SANE}}{1 - f_{\rm SANE}}, \tag{12}$$

where A_{π^0} is the inclusive π^0 asymmetry, and $f^p_{\pi^0}/f$ is the ratio of target dilution factors for π^0 production and electron scattering. The target dilution for electron scattering is defined in Equation 8, and the background target dilution, $f^p_{\pi^0}$, is similarly defined using cross sections for inclusive π^0 production. This ratio can be roughly approximated as unity ($f^p_{\pi^0}/f \simeq 1$) as it is well within the systematic uncertainties.

Simulations of the π^0 background and inclusive electron scattering were employed to determine $f_{\rm SANE}$ which is shown in Figure 22. A FORTRAN routine to model inclusive pion production by J. O'Connell [38] was updated using photoproduction cross section data from the Yerevan Physics Institute [39] to improve the cross section reproduction to better than 15% in the kinematics of interest. The updated pion production model also displayed good agreement when compared to charged pion electroproduction data [40]. The asymmetry of the pair-symmetric background, A_{π^0}, was estimated from fits to charged pion, parallel and transverse, asymmetry data taken on polarized $^{15}NH_3$ in SLAC experiments E143 and E155x. Data for both pion charges were averaged as a substitute for π^0. See Appendix A for a further discussion of the pion asymmetries.

6.3. Beam and target systematic errors

Table 3 shows an overview of SANE systematic error contributions from the beam and target systems, which enter Equation 4 as kinematics independent normalizations, and the kinematics dependent dilution factor. The error in the target polarization was the single largest contribution, and stems from the NMR polarization measurements. The NMR can be affected by minute shifts in the material beads over time and topological differences in dose accumulation around the coils embedded in the material. The thermal equilibrium measurements on which the enhanced NMR signals were calibrated also add error, with the temperature measurement of the material contributing significantly. Looking at the differences in the TE measurements over the experimental life of any given material gives an indication of the error. For example, material four's 3 TE measurements had a standard deviation of 8% around their mean, while material five had the same number of TE's with a 2% standard deviation. A detailed discussion of error in DNP targets from the SMC collaboration can be found in reference [41].

The global error in the beam polarization measurements contributes 1%, while the fit used to apply the measurements at varied beam energies will add another half percent. The dilution factor's uncertainty is based on statistical error in the measurement of the packing fraction and from the simulation.

Source	Error on Asymmetry
Beam polarization	1.5%
Target polarization	5.0%
Nitrogen correction	0.4%
Dilution factor	2.0%
Combined	5.6%

Table 3: Table showing systematic errors from the polarized beam and target.

7. Conclusion

Through a combination of a novel, wide-acceptance electron arm, and a rotatable, solid polarized proton target, the Spin Asymmetries on the Nucleon Experiment has significantly expanded the world's inclusive spin structure data for the proton. By taking spin asymmetry measurements with the target oriented at parallel and near perpendicular, model-independent access to virtual

Compton asymmetries A_1^p and A_2^p on the proton was possible with the only input being the well measured ratio of longitudinal to transverse unpolarized cross sections R_p. The only other sources of model independent proton A_1 measured in the same experiment are SLAC's E143 at 29 GeV [42] and E155 at 48 GeV [7], and the JLab's RSS [10]. SANE's kinematic coverage (shown in Figure 23) represents a crucial improvement to the world's data of inclusive proton scattering, particularly with a perpendicular target, filling in gaps in x coverage to allow integration for moments of structure functions, such as d_2. Forthcoming letters will present the physics results of these efforts.

Acknowledgements

We would like to express our sincerest gratitude to the staff and technicians of Jefferson Lab for their indispensable support during the running of SANE. We especially thank the Hall C and Target Group personnel, who saw a technically challenging experiment through significant hardship to a successful end. This material is based upon work supported by the U.S. Department of Energy, Office of Science, Office of Nuclear Physics under contract DE-AC05-06OR23177. This work was also supported by DOE grants DE-FG02-94ER4084 and DE-FG02-96ER40950.

Appendix A. Inclusive pion asymmetries

The SANE experiment directly measured the π^0 spin asymmetries in both field directions and at both beam energies [43]. The event selection criterion for π^0 events was two clusters in the calorimeter with a minimum separating distance of 20 cm, each cluster having greater than 0.6 GeV energy, and no signal in the Cherenkov detector. The π^0 energy ranged from 1.2 to 2.75 GeV. With the limited statistics, spin asymmetries were calculated by integrating the entire kinematic coverage in angle and energy. In Fig A.24, the π^0 spin asymmetries are plotted as a function of the experiment's run number for both beam energies and field directions. Combining data from both beam energies, the weighted average of the nearly perpendicular (A_{80}) and anti-parallel (A_{180}) asymmetries are 0.015 $\pm$ 0.019 and -0.020 $\pm$ 0.040, respectively. The weighted averages are plotted in Figure A.24 as a red solid (a violet dashed) line with the error band shown by the shaded box for A_{180} (A_{80}).

Given the limited statistics of the SANE measurement for the inclusive pion asymmetry, data from previous experiments was used to determine the inclusive pion asymmetry needed for background subtraction. The spin structure experiments at SLAC (E143 [42], E155 [7], E155x [8]) took inclusive charged pion data as part of their systematic background studies. In addition, E155 took dedicated data on longitudinal hadron and pion asymmetries [44]. The SLAC experiments measured spin asymmetries for target field directions that were parallel and nearly perpendicular (at 92.4°) to the beam directions. The data sets were taken from references [45] and [46].

The inclusive pion spin asymmetries can be parametrized as a function of the pion transverse momentum, $P_T = p_\pi \sin(\theta_\pi)$, where p_π and θ_π are the pion's outgoing momentum and angle. The SLAC data is taken at larger pion momentum (between 10 to 30 GeV/c) and small forward angles (2.75° to 7°) while the SANE data is taken at smaller pion momentum (between 1.2 and 2.75 GeV/c) and larger angles (between 30° and 50°). Therefore, the SANE and SLAC experiments cover a comparable range of P_T. The π^0 background for the SANE experiment has a lower limit of $P_T \approx 0.75$ GeV.

The SLAC charged pion inclusive parallel spin asymmetries are plotted as a function of P_T in Fig A.25. The parallel data do not show any significant dependence on P_T and the weighted average of the data has a χ-squared per degree of freedom below one. The weighted average of the SLAC parallel asymmetry, A_0 data is 0.024 $\pm$ 0.002 and is plotted as a solid red line in Fig A.25 with the error band shown by the shaded box. The SANE experiment used ^{14}N in the ammonia target and SLAC used ^{15}N, so the SLAC asymmetry needs to be multiplied by 14/15 to be compared with the SANE measurement. In addition, the parallel target field was at 180° for SANE compared to 0°, so for SANE the asymmetry becomes -0.022 $\pm$ 0.002. The π^0 parallel asymmetry measure by

SANE agrees with the SLAC measurement, but the SANE result has a much larger error bar. For the purpose of π^0 background subtraction discussed in Sec. 6.2.6, the SLAC weighted average was used.

The SLAC charged pion inclusive near perpendicularly spin asymmetries are plotted as a function of P_T in Fig A.26. The data do not show any significant dependence on P_T above 0.8 GeV/c and the weighted average of the data has a χ-squared per degree of freedom below one. The weighted average of the SLAC data (corrected for ^{14}N) is $A_{92.4} = -0.0012 \pm 0.0016$ and is plotted as a solid red line in Fig A.26 with the error band shown by the shaded box. The perpendicular asymmetry at 90°, A_{90}, is equal to $[A_{92.4} - A_0 \cos(92.4)]/\sin(92.4)$. Using the SLAC A_0 , then $A_{90} = -0.0003 \pm 0.0016$. For the background subtraction discussed in Sec. 6.2.6, A_{90} was taken to be zero and the error was applied part of overall systematic uncertainty.

References

[1] C. W. Leemann, D. R. Douglas, G. A. Krafft, The continuous electron beam accelerator facility: CEBAF at the Jefferson Laboratory, Annual Review of Nuclear and Particle Science 51 (1) (2001) 413–450. doi:10.1146/annurev.nucl.51.101701.132327.
URL https://doi.org/10.1146/annurev.nucl.51.101701.132327

[2] C. Yan, P. Adderley, R. Carlini, C. Cuevas, W. Vulcan, R. Wines, Target raster system at CEBAF, Nuclear Instruments and Methods in Physics Research Section A 365 (1) (1995) 46 – 48. doi:10.1016/0168-9002(95)00504-8.
URL http://www.sciencedirect.com/science/article/pii/0168900295005048

[3] M. Fukuda, S. Okumura, K. Arakawa, Simulation of spiral beam scanning for uniform irradiation on a large target, Nuclear Instruments and Methods in Physics Research Section A 396 (1–2) (1997) 45 – 49.

doi:10.1016/S0168-9002(97)00740-7.
URL http://www.sciencedirect.com/science/article/pii/S0168900297007407

[4] M. Hauger, et al., A high-precision polarimeter, Nuclear Instruments and Methods in Physics Research Section A: Accelerators, Spectrometers, Detectors and Associated Equipment 462 (3) (2001) 382 – 392. doi:https://doi.org/10.1016/S0168-9002(01)00197-8.
URL http://www.sciencedirect.com/science/article/pii/S0168900201001978

[5] A. Puckett, et al., Recoil Polarization Measurements of the Proton Electromagnetic Form Factor Ratio to $Q^2 = 8.5\ GeV^2$, Phys. Rev. Lett. 104 (24) (2010) 242301. doi:10.1103/PhysRevLett.104.242301.

[6] D. Crabb, D. Day, The Virginia/Basel/SLAC polarized target: operation and performance during experiment E143 at SLAC, Nuclear Instruments and Methods in Physics Research Section A: Accelerators, Spectrometers, Detectors and Associated Equipment 356 (1) (1995) 9 – 19, proceedings of the Seventh International Workshop on Polarized Target Materials and Techniques. doi:10.1016/0168-9002(94)01436-1.
URL http://www.sciencedirect.com/science/article/pii/0168900294014361

[7] P. L. Anthony, et al., Measurement of the proton and deuteron spin structure functions g_2 and asymmetry A_2, Phys. Lett. B458 (1999) 529–535. arXiv:hep-ex/9901006, doi:10.1016/S0370-2693(99)00590-0.

[8] P. L. Anthony, et al., Precision measurement of the proton and deuteron spin structure functions g_2 and asymmetries A_2, Phys. Lett. B553 (2003) 18–24. arXiv:hep-ex/0204028, doi:10.1016/S0370-2693(02)03015-0.

[9] H. Zhu, et al., Measurement of the electric form factor of the neutron through $d(e, en)p$ at Q2 = 0.5 GeV/c, Phys. Rev. Lett. 87 (2001) 081801.

doi:10.1103/PhysRevLett.87.081801.
URL http://link.aps.org/doi/10.1103/PhysRevLett.87.081801

[10] M. K. Jones, et al., Proton G_E/G_M from beam-target asymmetry, Phys. Rev. C 74 (2006) 035201. doi:10.1103/PhysRevC.74.035201.
URL https://link.aps.org/doi/10.1103/PhysRevC.74.035201

[11] J. Pierce, J. Maxwell, et al., Dynamically polarized target for the and experiments at jefferson lab, Nuclear Instruments and Methods in Physics Research Section A 738 (2014) 54 – 60. doi:10.1016/j.nima.2013.12.016.
URL http://www.sciencedirect.com/science/article/pii/S0168900213016999

[12] D. G. Crabb, W. Meyer, Solid polarized targets for nuclear and particle physics experiments, Annual Review of Nuclear and Particle Science 47 (1) (1997) 67–109. doi:10.1146/annurev.nucl.47.1.67.
URL http://arjournals.annualreviews.org/doi/abs/10.1146/annurev.nucl.47.1.67

[13] A. Abragam, M. Goldman, Principles of dynamic nuclear polarisation, Reports on Progress in Physics 41 (3) (1978) 395.
URL http://stacks.iop.org/0034-4885/41/i=3/a=002

[14] T. Maly, et al., Dynamic nuclear polarization at high magnetic fields, The Journal of Chemical Physics 128 (5) (2008) 052211. doi:10.1063/1.2833582.
URL https://doi.org/10.1063/1.2833582

[15] M. Borghini, Dynamic polarization of nuclei by electron-nucleus dipolar coupling ("effet solide"), Phys. Rev. Lett. 16 (1966) 318–322. doi:10.1103/PhysRevLett.16.318.
URL https://link.aps.org/doi/10.1103/PhysRevLett.16.318

[16] G. Court, D. Gifford, P. Harrison, W. Heyes, M. Houlden, A high precision Q-meter for the measurement of proton polarization in polarised targets,

Nuclear Instruments and Methods in Physics Research Section A 324 (3) (1993) 433 – 440. doi:10.1016/0168-9002(93)91047-Q.
URL http://www.sciencedirect.com/science/article/B6TJM-473FMTD-1BK/2/5df9fda11126f56afe51ffd03ead5dd2

[17] A. Abragam, The Principles of Nuclear Magnetism, Clarendon Press, Oxford, 1961.

[18] W. Meyer, Ammonia as a polarized solid target material–a review, Nuclear Instruments and Methods in Physics Research Section A 526 (1-2) (2004) 12 – 21. doi:10.1016/j.nima.2004.03.145.
URL http://www.sciencedirect.com/science/article/B6TJM-4C5G5R2-3/2/cbecc65cfb7729cc30f8f750cd77f05b

[19] T. J. Liu, T. D. Averett, D. G. Crabb, D. B. Day, J. S. McCarthy, O. A. Rondon, Depolarization of dynamically polarized solid targets due to beam heating effects, Nuclear Instruments and Methods in Physics Research Section A 405 (1) (1998) 1 – 12. doi:10.1016/S0168-9002(97)01211-4.
URL http://www.sciencedirect.com/science/article/B6TJM-41FDHH0-15/2/b585a02abd712c22ac208d15f5c90cd8

[20] P. M. McKee, Observations of radiation damage and recovery in ammonia targets, Nuclear Instruments and Methods in Physics Research Section A 526 (1-2) (2004) 60 – 64, proceedings of the ninth International Workshop on Polarized Solid Targets and Techniques. doi:10.1016/j.nima.2004.03.151.
URL http://www.sciencedirect.com/science/article/B6TJM-4C5G5R2-7/2/840ba4d447cd6eb87f040aa8c6a9b9c8

[21] J. Maxwell, Probing Proton Spin Structure: A Measurement of g_2^p at Four-momentum Transfer of 2 to 6 GeV^2, Ph.D. thesis, University of Virginia (2017). arXiv:1704.02308, doi:10.2172/1350087.
URL https://inspirehep.net/record/1590296/files/arXiv:1704.02308.pdf

[22] G. Warren, et al., Pr-03-002: Spin asymmetries on the nucleon experiment (sane), TJNAF Proposal.
URL https://misportal.jlab.org/mis/physics/experiments/viewProposal.cfm?paperId=123

[23] D. J. Hamilton, et al., Polarization transfer in proton compton scattering at high momentum transfer, Phys. Rev. Lett. 94 (2005) 242001. doi:10.1103/PhysRevLett.94.242001.
URL https://link.aps.org/doi/10.1103/PhysRevLett.94.242001

[24] A. J. R. Puckett, et al., Polarization transfer observables in elastic electron-proton scattering at $Q^2 = 2.5, 5.2, 6.8$, and $8.5 \mathrm{gev}^2$, Phys. Rev. C 96 (2017) 055203. doi:10.1103/PhysRevC.96.055203.
URL https://link.aps.org/doi/10.1103/PhysRevC.96.055203

[25] W. R. Armstrong, Measurement of the proton A_1 and A_2 spin asymmetries: Probing Color Forces, Ph.D. thesis, Temple U. (2015).
URL https://misportal.jlab.org/ul/publications/downloadFile.cfm?pub_id=13921

[26] W. R. Armstrong, S. Choi, E. Kaczanowicz, A. Lukhanin, Z.-E. Meziani, B. Sawatzky, A threshold gas cherenkov detector for the spin asymmetries of the nucleon experiment, Nuclear Instruments and Methods in Physics Research Section A 804 (2015) 118 – 126. doi:10.1016/j.nima.2015.09.050.
URL http://www.sciencedirect.com/science/article/pii/S0168900215011055

[27] A. P. Habarakada Liyanage, Proton form factor ratio, $\mu_p G_E^P / G_M^P$ from double spin asymmetry, Ph.D. thesis, Hampton U. (2013).
URL https://misportal.jlab.org/ul/publications/downloadFile.cfm?pub_id=12790

[28] H. Kang, Study of Double Spin Asymmetries in Inclusive ep Scattering at Jefferson Lab, Ph.D. thesis, Seoul Natl. U. (2014).

URL https://misportal.jlab.org/ul/publications/downloadFile.cfm?pub_id=13922

[29] E. Jastrzembski, et al., The jefferson lab trigger supervisor system, in: 1999 IEEE Conference on Real-Time Computer Applications in Nuclear Particle and Plasma Physics., 1999, pp. 538–542. doi:10.1109/RTCON.1999.842691.

[30] M. E. Christy, P. E. Bosted, Empirical fit to precision inclusive electron-proton cross sections in the resonance region, Phys. Rev. C 81 (2010) 055213. doi:10.1103/PhysRevC.81.055213.
URL https://link.aps.org/doi/10.1103/PhysRevC.81.055213

[31] R. H. Byrd, P. Lu, J. Nocedal, C. Zhu, A limited memory algorithm for bound constrained optimization, SIAM Journal on Scientific Computing 16 (5) (1995) 1190–1208. doi:10.1137/0916069.

[32] A. Liyanage, et al., Proton form factor ratio $\mu_p g_e^p / g_m^p$ from double spin asymmetry, In preparation.

[33] H. Kang, et al., Measurement of the transverse spin structure of the proton at medium to low momentum transfer, In preparation.

[34] P. E. Bosted, M. E. Christy, Empirical fit to inelastic electron-deuteron and electron-neutron resonance region transverse cross sections, Phys. Rev. C 77 (2008) 065206. doi:10.1103/PhysRevC.77.065206.
URL https://link.aps.org/doi/10.1103/PhysRevC.77.065206

[35] O. Rondon, The packing fraction and dilution factor in rss, Tech. rep., Technical report, Univ. of Virginia (2006).

[36] B. Adeva, et al., Measurement of proton and nitrogen polarization in ammonia and a test of equal spin temperature, Nuclear Instruments and Methods in Physics Research Section A 419 (1) (1998) 60 – 82. doi:10.1016/S0168-9002(98)00916-4.

URL http://www.sciencedirect.com/science/article/pii/S0168900298009164

[37] O. A. Rondon, Corrections to nucleon spin structure asymmetries measured on nuclear polarized targets, Phys. Rev. C 60 (3) (1999) 035201. doi:10.1103/PhysRevC.60.035201.

[38] J. O'Connell, Predicting inclusive electropion and nucleon cross sections for high particle momenta, National Bureau of Standards.

[39] K. V. Alanakyan, M. D. Amaryan, R. A. Demirchyan, K. S. Egiyan, D. V. Karumyan, Z. L. Kocharova, M. S. Ogandzhanyan, Y. G. Sharabyan, Spectra of π mesons in an inclusive reaction γC$\rightarrow\pi$X induced by bremsstrahlung γ quanta with a maximum energy of 4.5 GeV, ZhETF Pisma Redaktsiiu 32 (1980) 666. doi:10.17182/hepdata.18460.

[40] F. Heimlich, G. Huber, E. Rössle, F. David, H. Mommsen, D. Wegener, Production of negative pions from hydrogen, deuterium and carbon by high-energy electrons, Nuclear Physics A 267 (Supplement C) (1976) 493 – 502. doi:https://doi.org/10.1016/0375-9474(76)90674-6.
URL http://www.sciencedirect.com/science/article/pii/0375947476906746

[41] D. Adams, B. Adeva, et al., The polarized double cell target of the SMC, Nuclear Instruments and Methods in Physics Research Section A: Accelerators, Spectrometers, Detectors and Associated Equipment 437 (1) (1999) 23 – 67. doi:10.1016/S0168-9002(99)00582-3.
URL http://www.sciencedirect.com/science/article/pii/S0168900299005823

[42] K. Abe, et al., Measurements of the proton and deuteron spin structure functions g_1 and g_2, Phys. Rev. D 58 (11) (1998) 112003. doi:10.1103/PhysRevD.58.112003.

[43] L. Z. Ndukum, The extraction of the spin structure function, g_2 (and g_1) at low Bjorken x, Ph.D. thesis, Mississippi State U. (2015).
URL https://misportal.jlab.org/ul/publications/downloadFile.cfm?pub_id=13854

[44] P. L. Anthony, et al., Inclusive hadron photoproduction from longitudinally polarized protons and deuterons, Phys. Lett. B458 (1999) 536–544. arXiv:hep-ph/9902412, doi:10.1016/S0370-2693(99)00589-4.

[45] T. Toole, A precision measurement of the spin structure function g1p and g1d, Ph.D. thesis, American U. (2000).
URL https://www.slac.stanford.edu/exp/e155/e155_results/theses/toole_thesis_e155.pdf

[46] N. Benmouna, A precision measurement of the spin structure function g2p, Ph.D. thesis, American U. (2001).
URL http://www-public.slac.stanford.edu/sciDoc/docMeta.aspx?slacPubNumber=slac-r-616.html

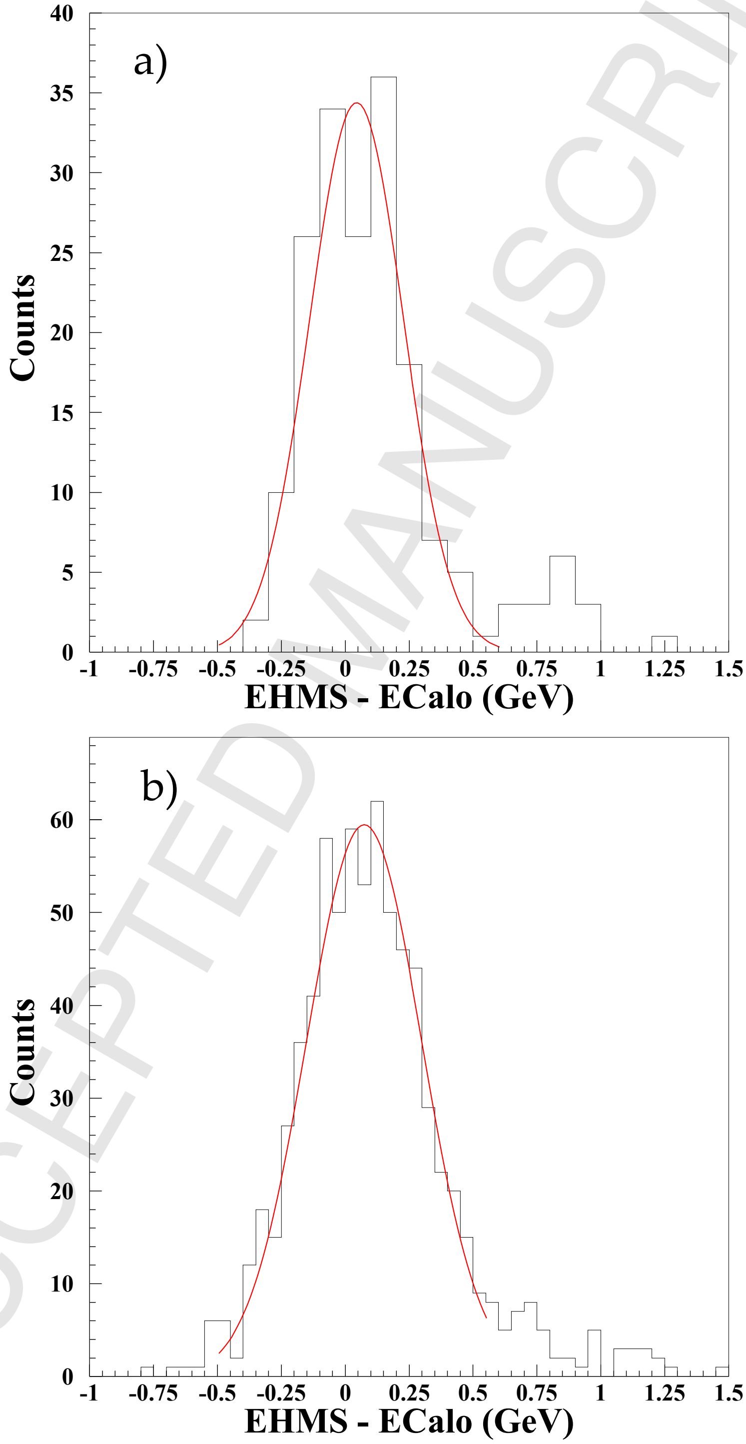

Figure 13: The difference of electron energies reconstructed from elastic protons detected in the HMS and the measured energies in BETA for 4.7 GeV (a) and 5.9 GeV (b) beam energies.

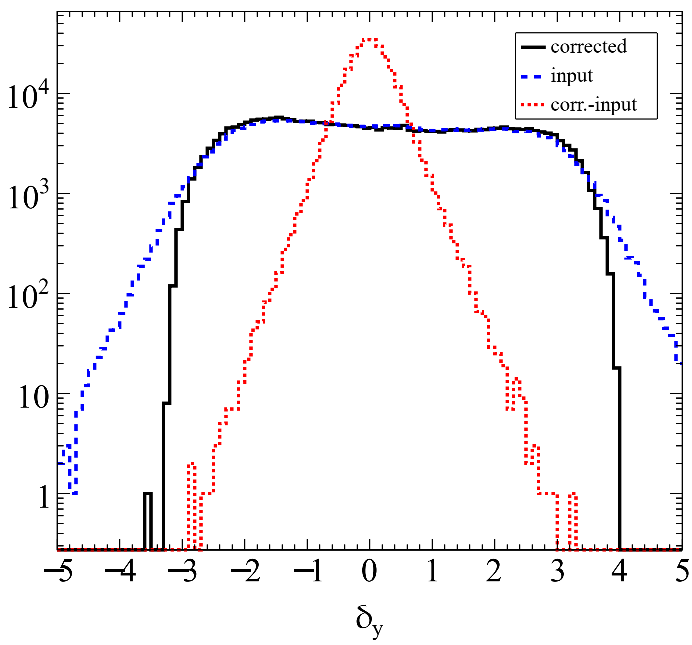

Figure 14: The performance of the network correction on the cluster y position (in cm). The blue (long dash) histogram shows the simulation input data used to train the network. The black (solid) histogram shows the network result. The red (small dash) histogram shows the difference between the two.

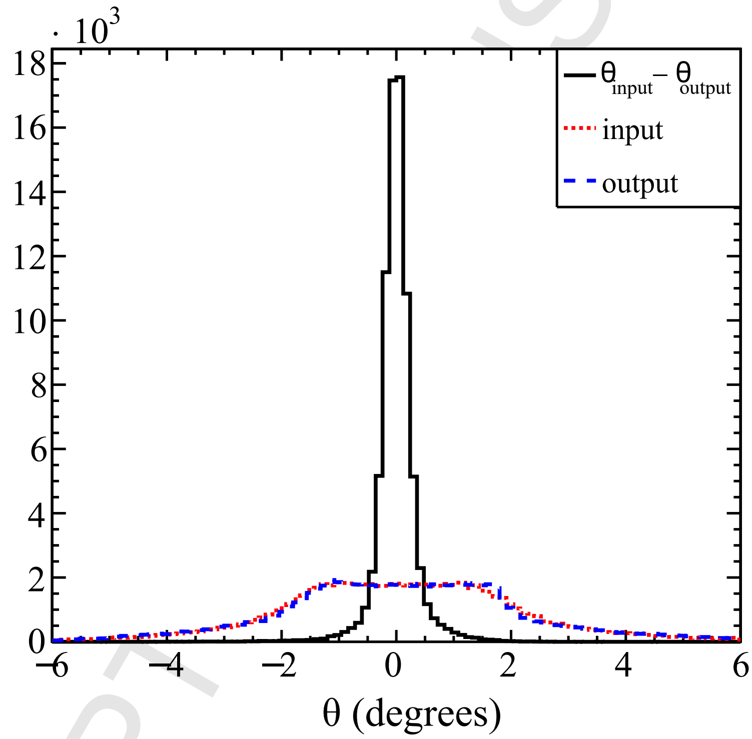

Figure 15: The performance of the network correction to calculate the physics scattering angle θ (in radians). The red histogram shows the simulation input data used to train the network. The blue histogram shows the trained network result and the black histogram shows the difference between the nominal (red, small dash) and network output (blue, long dash) results.

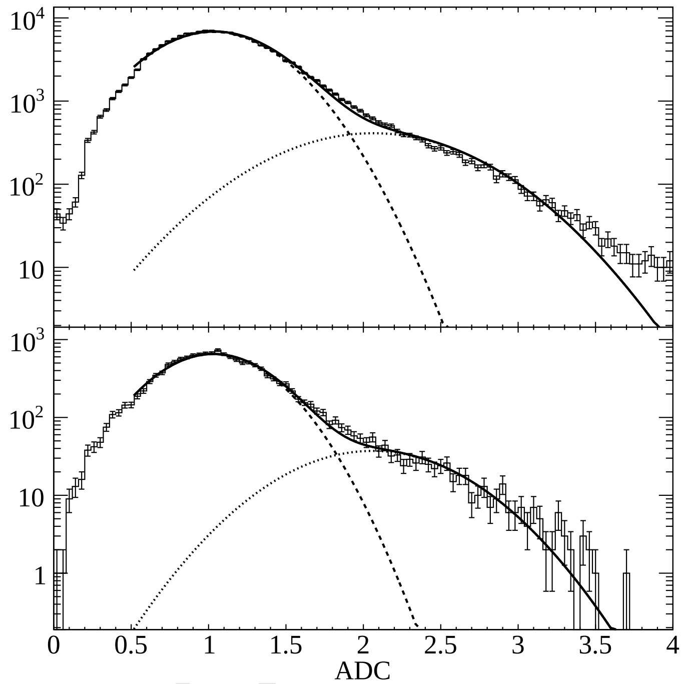

Figure 16: Cherenkov counter ADC spectrum for all the toroidal mirrors (top) and spherical mirrors (bottom).

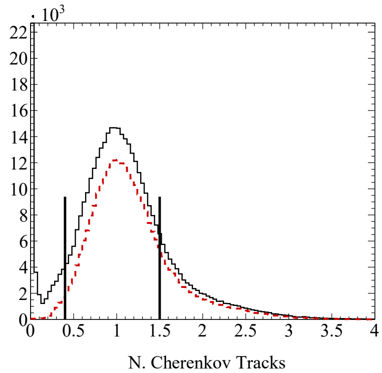

Figure 17: The Cherenkov ADC spectrum without (solid) and with (dotted) a TDC cut. The Cherenkov ADC window cut is defined by the vertical lines.

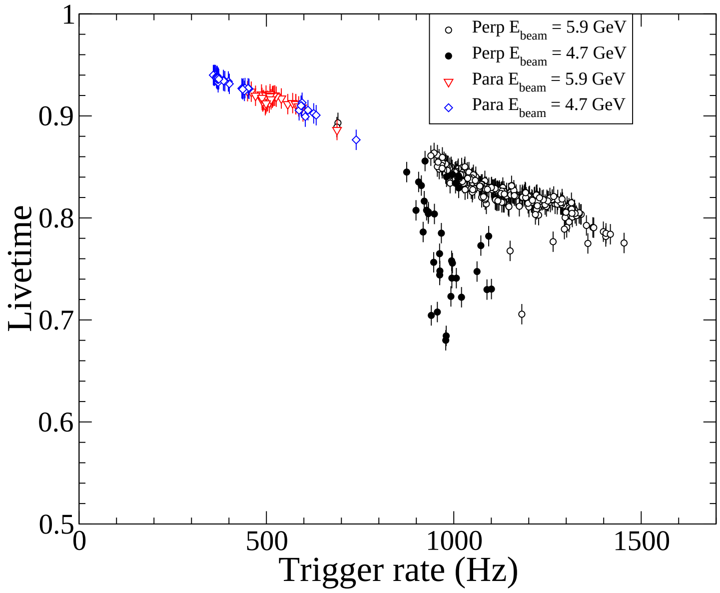

Figure 18: The computer livetime for negative helicity events as a function of negative helicity trigger rate.

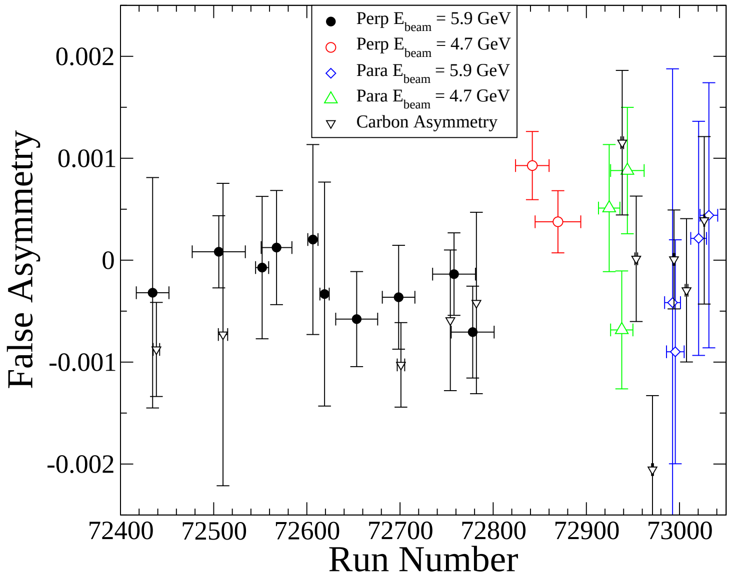

Figure 19: The false asymmetry for pairs of run groups with opposite sign of $P_B P_T$ versus run number.

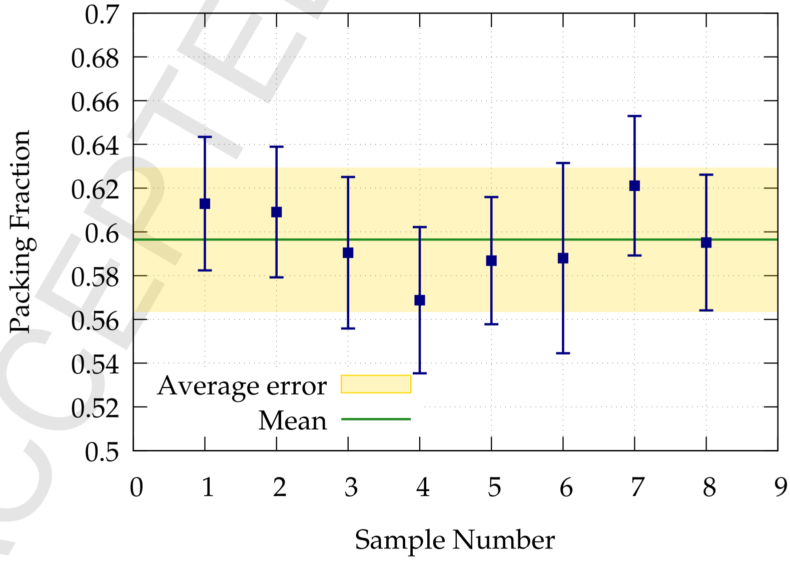

Figure 20: Packing fractions for all target material samples used during SANE, showing averaged value and error.

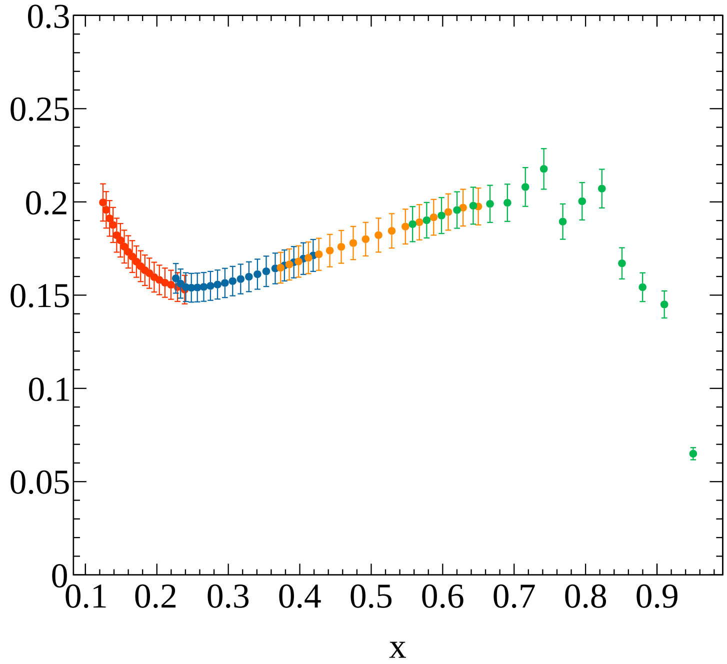

Figure 21: The dilution factor calculated for run 72925 as a function of x, showing the increasing contribution from the elastic tails at lower energies (i.e. lower x). Each color represents a different Q^2 bin.

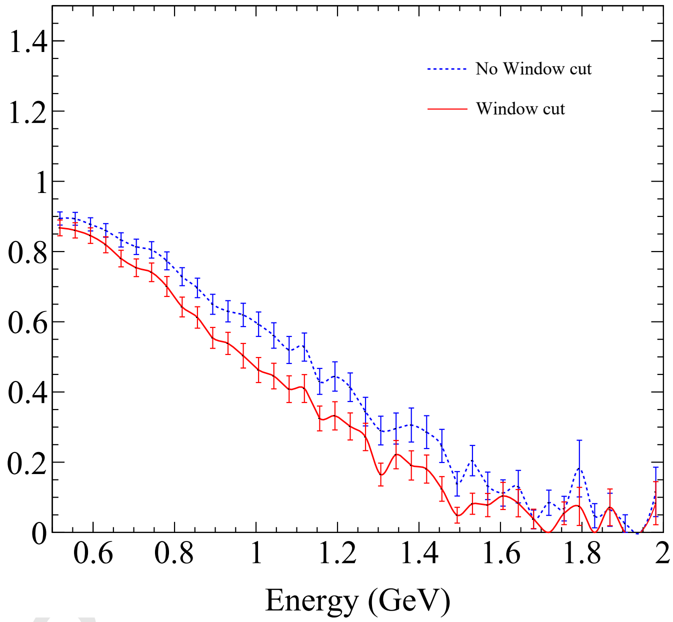

Figure 22: Simulations results for the pair symmetric background ratio f_{SANE} as a function of the scattered electron energy. The lower curve is the ratio with the Cherenkov ADC window which removes the background contributions from pairs converted in material outside of the target cell.

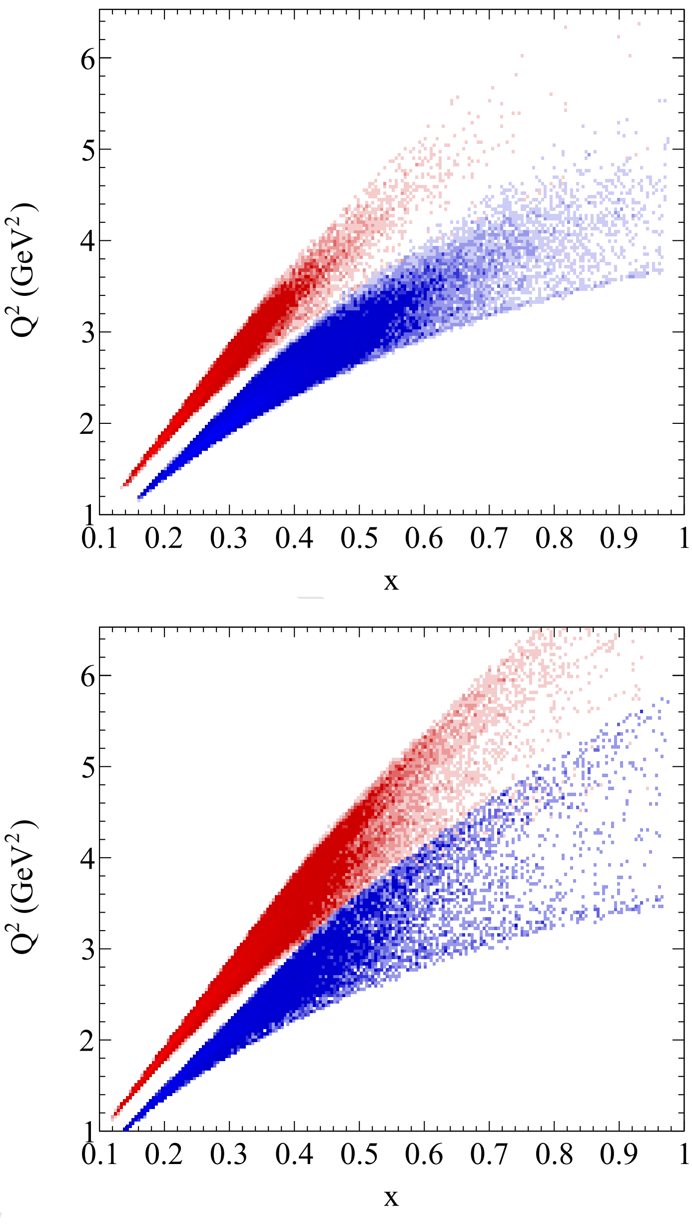

Figure 23: The kinematic coverage of SANE events, before cuts, with target oriented parallel (top) and at 80° to the beam (bottom). Red points represent 5.9 GeV beam energy coverage, while blue points show 4.8 GeV.

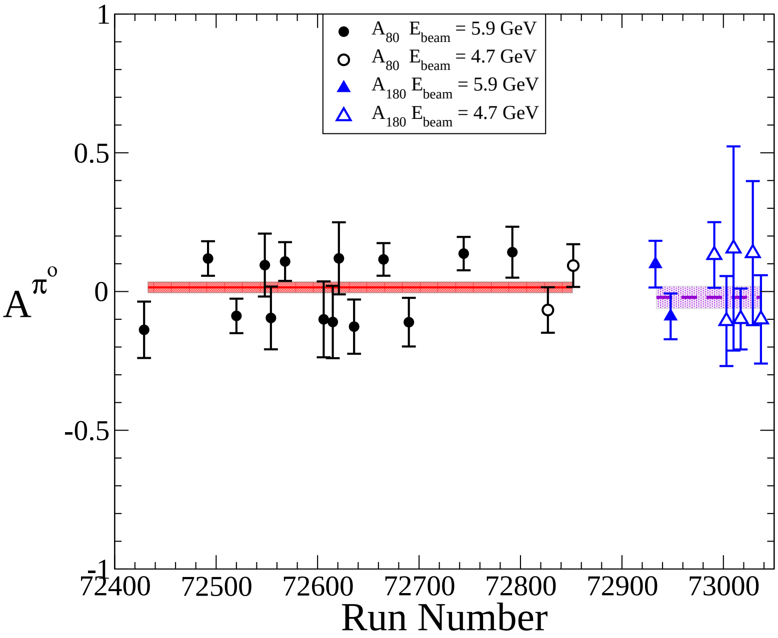

Figure A.24: The inclusive π^0 production spin asymmetry, A^{π^0}, plotted versus experiment's run number for anti-parallel, A_{180}, and nearly perpendicular, A_{80}, target field directions for both beam energies. Weighted averages and error bands for 180°(80°) asymmetries are shown as red solid (violet dashed) line and shaded box.

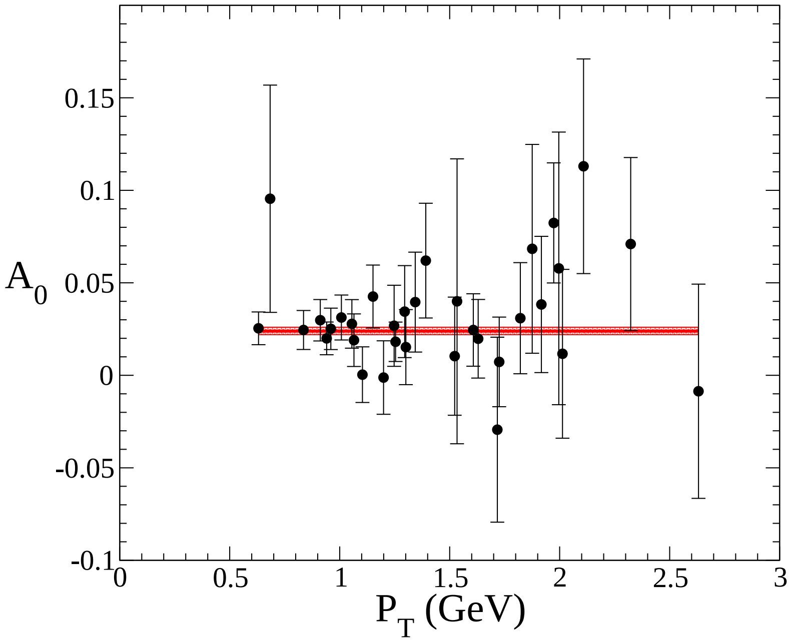

Figure A.25: SLAC pion production spin asymmetries for parallel target field direction plotted as a function of P_T. A weighted average is shown as a red line, with the error band as a shaded box.

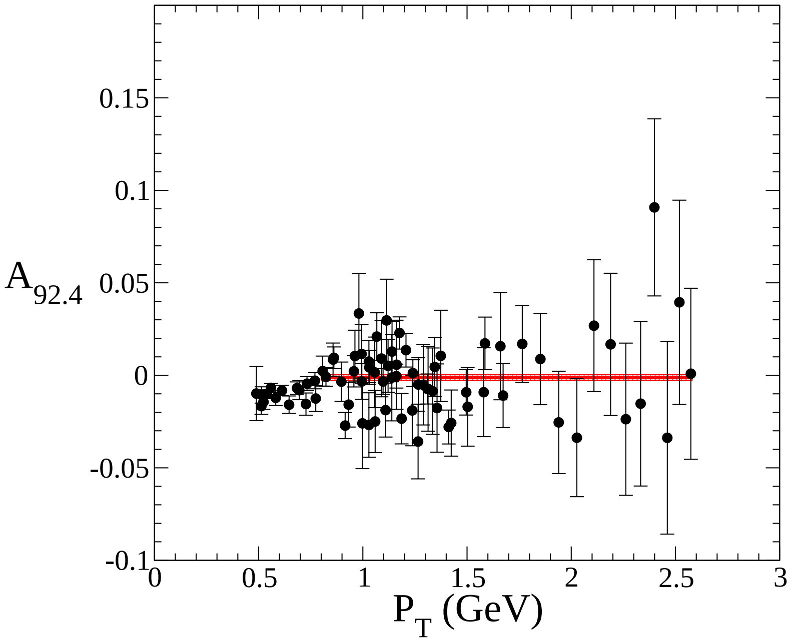

Figure A.26: SLAC pion production spin asymmetries for nearly perpendicular target field direction plotted as a function of P_T. A weighted average is shown as a red line, with the error band as a shaded box.